

# **Broadband Spectra Analysis of Three Energetic Millisecond Pulsars**

Department of Physics, The University of Hong Kong, Pokfulam  
Road, Hong Kong

Wang WenChao

3030053350

# Acknowledgements

This is acknowledgement.

# Abstract

In the thesis, I mainly introduce our study on the high energy spectra of three millisecond pulsars which are PSR J0218+4232, PSR B1821-24 and PSR B1937+21. The *Fermi Lat* Pass 8 data was published in 2015 and has lots of advantages over the old Pass 7 data, such as increased effective area and wider energy range. Since the recent gamma-ray spectra analysis of the three MSPs are relatively old (in about 2014), I redo the gamma-ray spectra analysis of the MSPs with 4-year more *Fermi Lat* observation data and newly published Pass 8 data. As expected, I obtain better fit results for gamma-ray spectra of the three MSPs with smaller errors and larger test statistic values. Then I briefly introduce a pulsar emission model called two-layer model [11] and do numerical simulation to test the two-layer model using the new observation data. By minimizing the differences between the predictions of the two-layer model and the real data, I fit the independent parameters of the two-layer model, which is helpful to understand emission mechanisms of pulsars. I find that though the two-layer model is simple, it can generate broad-band spectra of pulsars which are very close to the observation data from *Fermi Lat* in most energy bands.

# Contents

<b>Acknowledgements</b>	<b>i</b>
<b>Abstract</b>	<b>ii</b>
<b>List of Figures</b>	<b>iii</b>
<b>List of Tables</b>	<b>iii</b>
<b>1 Introduction</b>	<b>13</b>
1.1 Neutron Stars and Pulsars . . . . .	13
1.2 Emission Mechanism of Pulsars . . . . .	14
1.2.1 Magnetic Dipole Model . . . . .	15
1.2.2 Synchrotron Radiation . . . . .	16
1.2.3 Inverse-Compton radiation . . . . .	19
1.2.4 Curvature Radiation . . . . .	23
1.3 Millisecond Pulsar . . . . .	25

1.3.1	P- $\dot{P}$ Diagram . . . . .	25
1.3.2	Origin Of Millisecond Pulsars . . . . .	27
1.3.3	Class II MSPs . . . . .	28
1.4	Previous Work and Objectives . . . . .	29
<b>2</b>	<b>Gamma-Ray Analysis</b>	<b>31</b>
2.1	Introduction to the <i>Fermi Gamma-ray Space Telescope</i> . . . . .	31
2.2	A Brief Introduction to Fermi Data Analysis . . . . .	34
2.3	<i>Fermi Lat</i> Data Analysis . . . . .	37
2.3.1	Verifying the Data Analysis Process . . . . .	38
2.4	PSR J0218+4232 . . . . .	40
2.4.1	Count Maps And Count Cubes . . . . .	40
2.4.2	Binned Likelihood Analysis . . . . .	42
2.5	PSR B1821-24 . . . . .	45
2.5.1	Count Maps And Count Cubes . . . . .	46
2.5.2	Binned Likelihood Analysis . . . . .	48
2.6	PSR B1937+21 . . . . .	52
2.6.1	Phase Averaged Analysis . . . . .	52
2.6.2	Phase Resolved Analysis . . . . .	58

<b>3 Theory and Simulation</b>	<b>65</b>
3.1 A Brief Introduction to Outer Gap Model . . . . .	65
3.2 Two-layer Model . . . . .	67
3.3 Numerical Calculation of Spectra Based on Two-layer Model . .	72
3.4 Pitfalls and Considerations of Doing Numerical Calculation . . .	76
3.4.1 Correctness of Computation . . . . .	76
3.4.2 Speed of Computation . . . . .	77
<b>4 Conclusion</b>	<b>79</b>
<b>5 Discussion and Future Work</b>	<b>81</b>
5.1 Constraints of The Two-layer Model Used In The Thesis . . . .	81
5.2 Inconsistency Between the Two-layer Model and Fit Results . . . . .	82
5.3 Analysis With <i>LAT 8-year Point Source List</i> . . . . .	83

# List of Figures

1.1	Spatial distribution of some pulsars in galactic coordinate system.	14
1.2	Braking index of some pulsars. . . . .	16
1.3	Spectrum shape of synchrotron radiation for a single particle (top). According ot Equation 1.6, The top figure 1.6 describes the general shape of power spectrum of synchrotron radiation. When the frequency is larger than the critical frequency $\nu_c$ , the power goes down dramatically. However, the top figure does not show the information that at what frequency the charged particle emit the strongest power, which can be described in the bottom figure. The bottom figure reveals that most energy is emitted around critical frequency. . . . .	18
1.4	Inverse Compton Diagram . . . . .	20
1.5	Two photons collide with an electron. In the frame $S'$ , two photons collide with a rest electron successively. In the frame $S$ , the electron is no longer at rest and the positions of the two events are $x_1$ and $x_2$ . . . . .	24
1.6	Position of pulsars in P- $\dot{P}$ diagram . . . . .	26

1.7 A schematic diagram of Roche lobe. $L_1$ is called inner Lagrange point which is the intersection of equipotential lines of star A and B. . . . .	27
1.8 Pulse profiles of PSR B1937+21 in radio, X-ray and gamma-ray. [11] . . . . .	28
2.1 The figure ( <a href="https://www-glast.stanford.edu/instrument.html">https://www-glast.stanford.edu/instrument.html</a> ) illustrates how <i>Fermi Lat</i> tracks incident gamma-ray photons. . .	32
2.2 The count map of PSR J0218+4232 (left) and the count map generated by the model (right). In the left panel, the green circles represent sources needed to be fitted. The right panel is a count map created according to the fitted spectra model. The size of each figure is 141 pixels $\times$ 141 pixels, and the dimension for each pixel is $0.2^\circ \times 0.2^\circ$ . . . . .	41
2.3 Three count maps from PSR J0218+4232's count cube. The energy ranges of the figures are 100~123MeV, 1.873~2.310GeV, 35.11~43.29GeV respectively. . . . .	41



2.7	The count spectra and count residuals of PSR J0218+4232. The upper panel is the count spectrum of all sources included in the fit procedure. Thick lines are those sources with free fit parameters while the thin lines are fixed sources. The green line and the black dots represents observed counts in different energy bands. The purple line represents galactic emission. The lower panel shows the count residuals in different energy bands.	47
2.8	The count map of PSR B1821-24 (left) and the count map generated by the model (right). In the left panel, the green circles are free sources. The sizes of the both figures are 141 pixels $\times$ 141 pixels, and each pixel's dimension is $0.2^\circ \times 0.2^\circ$ .	47
2.9	Three figures of PSR B1821-24's count cube. The energy ranges of the figures are 100~123MeV, 1.873~2.310GeV, 81.11~100GeV respectively from left to right.	48
2.10	The count map and residual map of PSR B1821-24 in linear scale. The reason why use linear scale is not used here is that the residual map is nearly black in linear scale. The <b>left</b> figure is the count map and the <b>right</b> figure is the residual map showing the difference between the observation data and the spectral model.	48
2.11	The log-log plot of flux to energy of PSR B1821-24's gamma-ray spectrum.	49

2.12 TS maps of PSR B1821-24. The figures' dimensions are $4^\circ \times 4^\circ$ (20 pixels $\times$ 20 pixels with $0.2^\circ \times 0.2^\circ$ for each pixel). The left and right panels are generated by the XML models with and without the target source PSR B1821-24 respectively. The left panel shows that the possibility of adding an imputative point source is very low only with a maximum TS value of less than 11 while the TS values of the right figure are generally much larger. . . . .	50
2.13 The count spectra and count residuals of PSR B1821-24A. The upper panel is the count spectrum of all sources included in the fit procedure. Thick lines are those sources with free fit parameters while the thin lines are fixed sources. The green line and the black dots represents observed counts in different energy bands. The purple line represents galactic emission. The lower panel shows the count residuals in different energy bands. . . . .	51
2.14 The count maps of PSR B1937+21 created from observation data (left) and from the spectral model (right). The dimensions of both figures are $141\text{pixels} \times 141\text{pixels}$ and each pixel's size is $0.2^\circ \times 0.2^\circ$ . . . . .	53
2.15 Three count maps of PSR B1937+21's count cube. The energy ranges of the figures are from 100 to 131 MeV, from 2460 to 3212 MeV, from 12198 to 15929 MeV respectively. . . . .	53
2.16 The count map created from observation data (left) and residual map (right) of PSR B1937+21. Both left and right panels are in linear scale. The dimension is $141\text{pixels} \times 141\text{pixels}$ and each pixel's size is $0.2^\circ \times 0.2^\circ$ . . . . .	54

2.17 TS maps of PSR B1937+21. The dimension is $3^\circ \times 3^\circ$ (15 pixels $\times$ 15 pixels and each pixel is $0.2^\circ \times 0.2^\circ$ ). The left panel is generated by the model by removing PSR B1937+21 while the right panel contains the target source. . . . .	55
2.18 Top: count spectra for all sources included in the xml model (including sources with both free parameters and fixed parameters). Bottom: counts residual plot of the model. The thick red line is the target source PSR B1937+21, the blue thick lines are sources with free parameters and the thin lines are the sources with only fixed parameters. . . . .	56
2.19 Top panel is counts spectra for all sources within the ROI. Bottom panel shows the counts residual. . . . .	57
2.20 TS maps of PSR B1937+21 (power-law model). The dimension is $4^\circ \times 4^\circ$ (20 pixels $\times$ 20 pixels and each pixel is $0.2^\circ \times 0.2^\circ$ ). The left panel is generated by the model after removing PSR B1937+21 while the right panel contains the source. . . . .	57
2.21 The log-log plot of flux to energy of PSR B1937+21's gamma-ray spectrum. The red line represents the PLExpCutoff model and the green line is the power-law model. . . . .	58
2.22 Top left panel shows the pulse phase of PSR B1937+21 in gamma-ray band. The figure is produced by tempo2. . . . .	59
2.23 Light curves of PSR B1937+21 by different telescopes. The data and figure is from the paper [6] . . . . .	59

2.24 The count maps of PSR B1937+21 created from observation data ( <b>left</b> ) and from the spectral model ( <b>right</b> ). The dimensions of both figures are $141\text{pixels} \times 141\text{pixels}$ and each pixel's size is $0.2^\circ \times 0.2^\circ$ .	60
2.25 Three count maps of PSR B1937+21's count cube. The energy ranges of the figures are from 100 to 126 MeV, from 1.99 to 2.51 GeV, from 50.12 to 63.10 GeV respectively.	61
2.26 The count maps of PSR B1937+21 created from observation data ( <b>left</b> ) and from the spectral model ( <b>right</b> ). The dimensions of both figures are $141\text{pixels} \times 141\text{pixels}$ and each pixel's size is $0.2^\circ \times 0.2^\circ$ .	62
2.27 The count spectra (top) of all sources including those with only fixed parameters and count residuals (bottom) of the fit for PSR B1937+21.	63
2.28 PLExpCutoff model spectrum of PSR B1937+21 (phase resolved).	63
2.29 TS maps of PSR B1937+21. The dimension is $3^\circ \times 3^\circ$ (15 pixels $\times$ 15 pixels and each pixel is $0.2^\circ \times 0.2^\circ$ ). The left panel is generated by the model after removing PSR B1937+21 while the right panel contains the source.	64

3.1 (a): Geometry of the two-layer model. $h_1$ and $h_2$ is the height of the primary region and the screening region respectively. (b): the charge densities of primary region and screening region. In the primary region, the charge density is much smaller than Goldreich-Julian charge density while is larger in the screening region. The figure is from [16]. . . . .	68
3.2 The modeled spectrum of PSR J0218+4232. . . . .	73
3.3 The modeled spectrum of PSR B1821-24. . . . .	73
3.4 The modeled spectrum of PSR B1937+21. . . . .	74
3.5 The broad band and modeled spectrum of PSR J0218+4232. The grey shade is the error of the global fit. And the green shade in the left panel of the figure represents the error of hard X-ray. The 'Total' legend represents the total flux combining the Synchrotron radiation, inverse Compton radiation and curvature radiation altogether. . . . .	75
3.6 The broad band and modeled spectrum of PSR B1821-24. The meaning of grey shade and the green shade are the same as Figure 3.5 . . . . .	75
3.7 The broad band and modeled spectrum of PSR B1937+21. The meaning of grey shade and the green shade are the same as Figure 3.5 . . . . .	76

## List of Tables

1.1	A few intrinsic properties of PSRs J0218+4232, B1821-24 and B1937+21. The data is from ATNF Pulsar Catalogue. [12] . . . . .	29
1.2	A few intrinsic properties of PSRs J0218+4232, B1821-24 and B1937+21. [12] [11] [6] . . . . .	30
2.1	The spectra fit results. In the thesis, in order to make data analysis more convinient, I use some pipeline scripts to deal with the observation data. The "Test Results" column is the results generated by using the pipeline scripts. The "Previous Results" column lists the corresponding spectra properties based on the previous studies [2]. According to the standard PLExpCutoff model (described in equation 2.4, $\Gamma$ is photon index and $E_c$ is cutoff energy.) . . . . .	39
2.2	Fit results with data from year 2009 to year 2018. The physical meanings of $\Gamma$ and $E_c$ are the same as Table 2.1 . . . . .	39
2.3	Numbers of photon counts of count maps in different energy bands for PSR J0218+4232. . . . .	42

2.4	Fit parameters of the spectral model of PSR J0218+4232. The names of parameters are consistent with Equation 2.4. The previous results are from the paper [2]. . . . .	44
2.5	Fit parameters of the spectral model of PSR B1821-24. The names of parameters are also onsistent with Equation 2.4 The energy ranges of photon flux between the two results are different.	50
2.6	Fit parameters of the spectral model of PSR B1937+21. The names of parameters are consistent with Equation 2.4. The old results are from the paper [11]. Note that since the paper prefers power-law model than PLExpCutoff model, it does not report the photon flux of PLExpCutoff model. . . . .	54
2.7	Photon index comparison of power-law model between different studies. The data of column <i>Previous 1</i> is from the paper [11] and column <i>Previous 2</i> is from the paper [6]. . . . .	55
2.8	Fit parameters of the spectral model of PSR B1937+21 (phase resolved). The previous results are from the paper [11]. Since the studied energy range is different, I do not list the energy flux for comparison. . . . .	64
3.1	The results of fitting parameters for the three MSPs. The physical meaning of each parameter is consistent with the two-layer model describe above. . . . .	74
4.1	Fit parameters of the spectral model of PSR J0218+4232. The names of parameters are consistent with Equation 2.4. The previous results are from the paper [2]. . . . .	79



# Chapter 1

## Introduction

### 1.1 Neutron Stars and Pulsars

Neutron stars are produced by supernovae explosion of massive stars which have about four to eight solar mass. After a supernova explosion, a star leaves a central region. And the central region collapses because of the effect of gravity until protons and electrons combine to form neutrons ( $e^- + p \rightarrow n + \nu_e$ ) —the reason why they are called “neutron stars”. Because neutrons have no electromagnetic force on each other, they can be squeezed very tightly. Therefore, a neutron star has tremendous high density (about  $5 \times 10^{17} \text{ kg/m}^3$ ) and its diameter and mass is about 20km and 1.4 solar mass respectively. What prevents a neutron star to continue to contract is the degeneracy pressure of neutrons.

Pulsars are fast-spinning neutron stars. They have rotational periods from a few milliseconds to several seconds. For example, the rotational period of PSR B1937+21 is about 1.56ms while PSR B1919+21 is approximately 1.34s. As we know, a star can be ripped by centrifugal force if the star rotates too fast.

We can estimate lower limit of density of a star with the equation  $\rho = \frac{3\pi}{P^2 G}$ , where  $P$  is the rotational period of a pulsar. Just for simplicity, let  $P$  be 1s. Then we get  $\rho \approx 1.4 \times 10^{11} \text{ kg/m}^3$ . With the knowledge that the density of a white dwarf is about  $1 \times 10^9 \text{ kg/m}^3$  which is smaller than the lower density limit, the observed fast-spinning stars belong to the kind of stars which are much denser than white dwarf. As a result, neutron stars are ideal candidates for pulsars.

More than 2000 pulsars have been discovered so far. Most of them are in the disk of our Galaxy while we also can find a small portion of them in high latitude, which can be seen clearly in Figure 1.1. This may because they cannot escape the gravitational potential if their kinetic energy is not large enough. Besides, even though they have large enough velocities to escape from their birth region, there are some probabilities that they become nearly non-detectable before reaching high latitude.

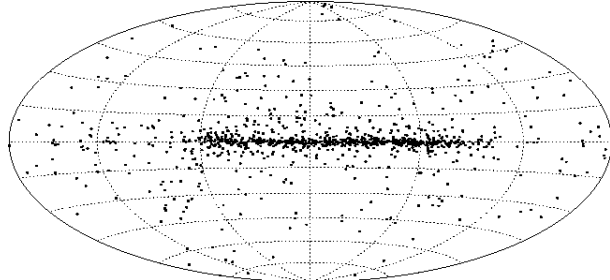


Figure 1.1: Spatial distribution of some pulsars in galactic coordinate system.

## 1.2 Emission Mechanism of Pulsars

Although the emission mechanism of pulsars has not been fully understood yet, some models have been developed trying to explain observational data. The following is a simple model that can explain some basic features of pulsars spectra. I will first introduce the magnetic dipole model, then the synchrotron

radiation and inverse Compton radiation.

### 1.2.1 Magnetic Dipole Model

Assuming a pulsar has a magnetic dipole moment  $\vec{m}$ , the angle between rotation axis and direction of  $\vec{m}$  is  $\alpha$ , its angular velocity is  $\Omega$ , radius is  $R$  and moment of inertia is  $I$ . Also assuming that energy of electromagnetic radiation is completely from the rotational energy, its spin-down rate can be written as:

$$\dot{\Omega} = -\frac{B_p^2 R^6 \Omega^3 \sin \alpha^3}{6c^3 I}$$

where  $B_p$  is magnetic field strength in the pole of the pulsar. Its surface magnetic field can also be estimated by:

$$B_s = \sqrt{\frac{3c^3 I}{2\pi^2 R^6} P \dot{P}} = 3.2 \times 10^{19} \sqrt{P \dot{P}}$$

where  $B_s$  is the strength of surface magnetic field.

In general, a pulsar's spin down rate can be expressed as:  $\dot{\Omega} = -K\Omega^n$ , where  $K$  is a constant and  $n$  is called braking index. In magnetic dipole model  $n$  is 3 [15]. Then characteristic age of the pulsar can be defined as:  $P/2\dot{P}$  in magnetic dipole model. For example, the Crab pulsar's rotation period is about  $0.033s$  and period derivative is  $4.22 \times 10^{-13}s/s$ . The characteristic age is about 1200 years. The pulsar is remnant of a supernova which is observed by ancient astronomers in 1054 AD, so the record shows that characteristic age can give us an order of magnitude estimate of a pulsar's real age.

Although the braking index is 3 in magnetic dipole model, most of pulsars' braking index is less than 3 as shown in Figure 1.2. The reason is that if a pulsar's spin down is completely because of pulsar wind, the braking index is 1. Thus, the real braking index should be a combination of 1 and 3, which is

usually less than 3. [8]

Pulsar	$n_{\text{obs}}$	$\Omega$ $\text{s}^{-1}$	$\dot{\Omega}$ $10^{-10}\text{s}^{-2}$
PSR B0531+21 (Crab)	$2.51 \pm 0.01$	$30.22543701$	$-3.862283$
PSR B0540-69	$2.14 \pm 0.01$	$19.8344965$	$-1.88383$
PSR B0833-45 (Vela)	$1.4 \pm 0.2$	$11.2$	$-0.157$
PSR B1509-58	$2.839 \pm 0.001$	$6.633598804$	$-0.675801754$
PSR J1846-0258	$2.16 \pm 0.13$	$3.0621185502$	$-0.6664350$
PSR J1833-1034	$1.857 \pm 0.001$	$16.159357$	$-0.5275017$
PSR J1119-6127	$2.684 \pm 0.001$	$2.4512027814$	$0.2415507$
PSR J1734-3333	$0.9 \pm 0.2$	$0.855182765$	$-0.0166702$

Figure 1.2: Braking index of some pulsars.

### 1.2.2 Synchrotron Radiation

Synchrotron radiation is a special case of cyclotron radiation when a particle's speed is comparable to the speed of light. Because of the relativistic beaming effect, we will observe a very short radiation pulse when speed of particles is large. We only aim to analyze the spectral properties of MSPs, so we focus on the spectrum property of synchrotron radiation. With Larmor's Formula we can derive the synchrotron radiation power of an electron:

$$P = \frac{2e^4\gamma^2\beta^2B_\perp^2}{3m_e^2c^3} \quad (1.1)$$

where  $\gamma$  is the Lorentz factor of the electron,  $\beta = v/c$  and  $B_\perp$  is the strength of magnetic field perpendicular to the circular motion plane. When  $\beta \sim 1$ , Function 1.1 can be simplified as:

$$P = \frac{2e^2c}{3R^2}\gamma^4 \quad (1.2)$$

where  $R = E/eB_\perp$  is the radius of the electron's circular motion. Furthermore, the power spectrum of a single electron can be described by Function 1.3

$$\begin{aligned} P(\nu) &= \frac{\sqrt{3}e^3 B \sin \alpha}{mc^2} \left( \frac{\nu}{\nu_c} \right) \int_{\nu/\nu_c}^{\infty} K_{5/3}(\eta) d\eta \\ &= \frac{\sqrt{3}e^2}{m_e R} \gamma \left( \frac{\nu}{\nu_c} \right) \int_{\nu/\nu_c}^{\infty} K_{5/3}(\eta) d\eta \end{aligned} \quad (1.3)$$

where  $\nu_c$  is the critical frequency and  $K_{5/3}$  is modified Bessel function. The critical frequency can be expressed by Function 1.4

$$\begin{aligned} \nu_c &= \frac{3}{2} \gamma^2 \nu_{cyc} \sin \alpha \\ &= \frac{3}{4\pi} \frac{c}{R} \gamma^3 \end{aligned} \quad (1.4)$$

where  $\alpha$  is the pitch angle and the  $\nu_{cyc}$  is the frequency of corresponding cyclotron radiation. These functions do not give us very much information because of the integration of the modified Bessel function. We let  $x = \nu/\nu_c$  and fix the environment variables such as magnetic field ( $B$ ), Function 1.3 becomes:

$$P(\nu) = C \times x \int_x^{\infty} K_{5/3}(\eta) d\eta \quad (1.5)$$

where  $C$  is a constant dependent on  $B$ . Thus, in order to analyze the power spectrum of synchrotron radiation, we only concentrate on the later part, which is

$$F(x) = x \int_x^{\infty} K_{5/3}(\eta) d\eta \quad (1.6)$$

In reality, synchrotron radiation is not generated by a single particle. We describe the number density distribution of electrons with respect to energy by a single power-law model:

$$N(E) \approx CE^{-\delta} \quad (1.7)$$

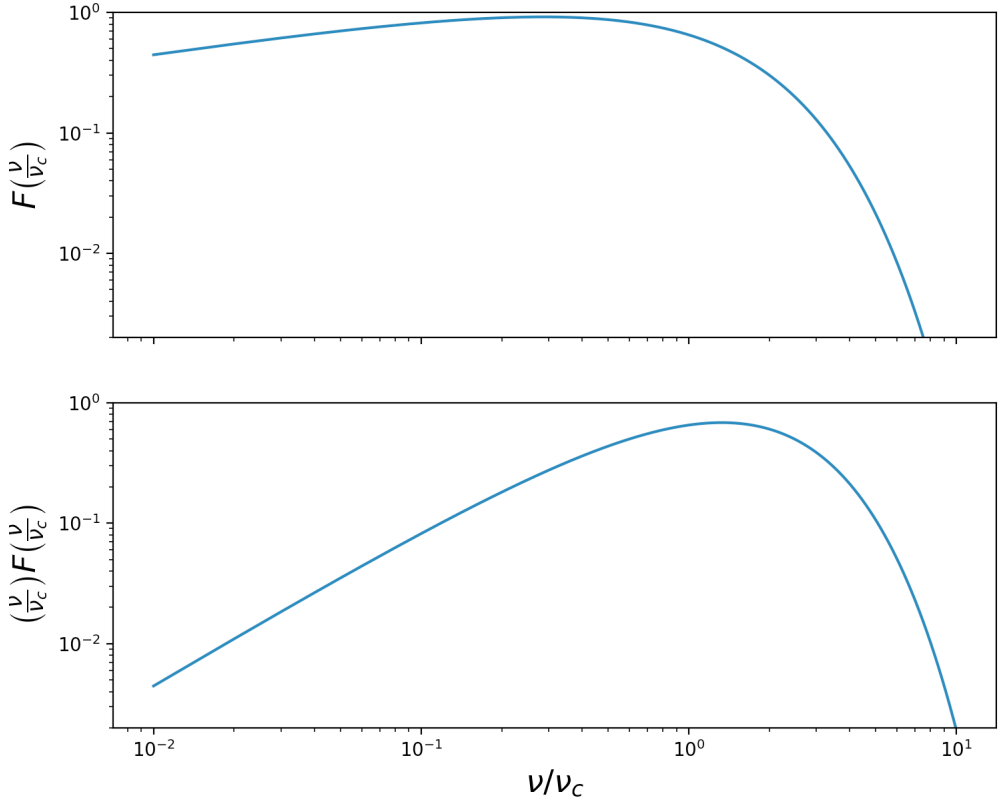


Figure 1.3: Spectrum shape of synchrotron radiation for a single particle (top). According to Equation 1.6, The top figure 1.6 describes the general shape of power spectrum of synchrotron radiation. When the frequency is larger than the critical frequency  $\nu_c$ , the power goes down dramatically. However, the top figure does not show the information that at what frequency the charged particle emit the strongest power, which can be described in the bottom figure. The bottom figure reveals that most energy is emitted around critical frequency.

For simplicity, we set the ambient magnetic field  $B$  to be a constant and make an approximation that all radiations are at a single frequency:

$$\nu \approx \gamma^2 \nu_{cyc} \quad (1.8)$$

where the meaning of  $\nu_{cyc}$  is the same as Function 1.4. Our objective is to know the relationship between total power of all electrons and their radiation frequency. We describe the relationship as Equation 1.9

$$-P(E)N(E)dE = Q_\nu d\nu \quad (1.9)$$

$$P(E) = \frac{4}{3}\sigma_T\beta^2\gamma^2cU_B \quad (1.10)$$

where  $\sigma_T$  is electron Thompson scattering section,  $U_B$  is energy density of the environment magnetic field,  $Q_{nu}$  is the emission coefficient of synchrotron radiation and  $E = \gamma m_e c^2$ . With Equation 1.8, we have

$$P = \frac{dE}{d\nu} = \frac{m_e c^2}{2\sqrt{\nu\nu_{cyc}}} \quad (1.11)$$

Combine Functions 1.11 and 1.9 we get:

$$Q_\nu = \frac{4}{3}\sigma_T\beta^2\gamma^2cU_B \frac{m_e c^2}{2\sqrt{\nu\nu_{cyc}}} N(E) \quad (1.12)$$

Ignoring constants in Function 1.9 we have

$$Q_\nu \propto \nu^{(1-\delta)/2} \quad (1.13)$$

Function 1.13 shows that if the number density electrons is a power-law distribution, the spectrum of synchrotron radiation is also a power-law model.

### 1.2.3 Inverse-Compton radiation

If an energetic relativistic photon collides with a charged particle from an proper incident angle, the photon's energy decreases and its direction changes. This is the process of Compton Scattering. Inverse-Compton radiation is the opposite process and a low energy photon gained energy from an ultra-relativistic electron in the process.

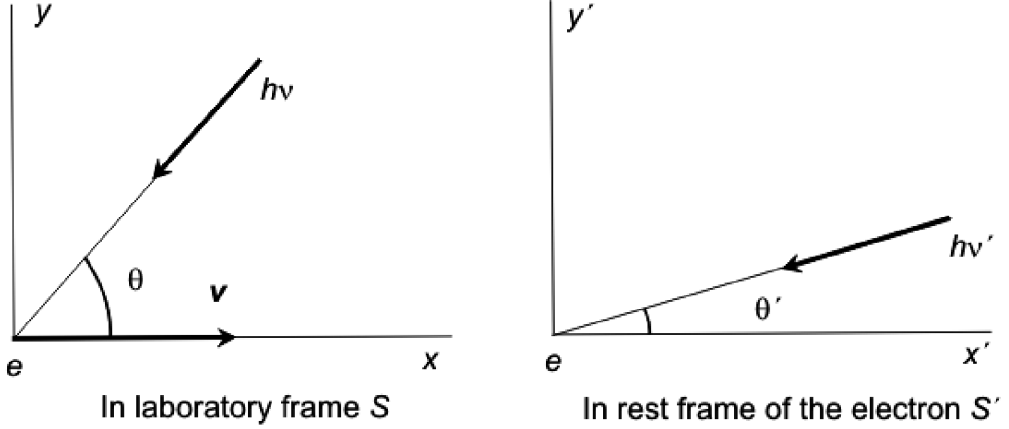


Figure 1.4: Inverse Compton Diagram

As Figure 1.4 shows, in the laboratory frame ( $S$ ), the incident angle and energy of a photon is  $\theta$  and  $h\nu$  respectively. The speed of the electron is  $v$ . In the electron rest frame ( $S'$ ), we change the denotation to  $\theta'$ ,  $h\nu'$  and. Also, let the position of the electron be the origin point of  $S'$ . We can study the whole process in the  $S'$  frame, the transfer the result to the  $S$  frame by Lorentz transformation.

In the  $S'$  frame, the electron is at rest so its energy is  $m_e c^2$ . For Inverse Compton scattering, the energy of an incident photon (less than several keV) is much less than the rest energy of an electron (about  $0.51 MeV$ ) and the relationship can be expressed by  $h\nu' \ll m_e c^2$ . Therefore, this can be treated as Thompson Scattering process. Let the Poynting vector of incident photons be  $\vec{S}'$  and their energy density be  $U'_{rad}$ , we have equation 1.14

$$\vec{S}' = c U'_{rad} \quad (1.14)$$

The electron absorbs the energy of the incident photons and then be accelerated. Thus the accelerated electron will emit part of the energy taken from incoming photons and the power of scattered radiation is denoted as  $P'$ . The

ratio can be described by Thompson Scattering cross section  $\sigma_T$  which is:

$$\sigma_T = \frac{8\pi}{3} \left( \frac{e^2}{m_e c^2} \right)^2 \quad (1.15)$$

and the relationship between the electron radiation power and incoming photon energy flux can be described by Equation 1.16

$$P' = \left| \vec{S}' \right| \sigma_T \quad (1.16)$$

Combine Eqs. 1.14 and 1.16, the radiation power emitted by the electron is:

$$P' = c \sigma_T U'_{rad} \quad (1.17)$$

Then we need to find the relationship between frames  $S$  and  $S'$ . It mainly contains two parts: the relationship between  $P$ ,  $P'$  and  $U_{rad}$ ,  $U'_{rad}$ . Since  $P = dE/dt$  and  $dE/dt$  is Lorentz invariant in inertial frame, we get the equation:

$$P = P' \quad (1.18)$$

Now we hope to write  $U'_{rad}$  in terms of  $U_{rad}$ .  $U_{rad}$  is comprised by energy of a single photon and photon density. In the following analysis, all the denotations are correspondent to Equation 1.4. According to the relativistic Doppler shift formula, we have:

$$h\nu' = (h\nu) \gamma (1 + \beta \cos \theta) \quad (1.19)$$

where  $\beta = v/c$  and  $\gamma$  is Lorentz factor of an ultra-relativistic electron. Then we calculate the photon density. In the frame  $S'$ , the photon density is inverse proportional to the time interval ( $\Delta t$ ) between the two photons striking the electron since total number of photons is Lorentz invariant. In laboratory

frame  $S$ , we consider two photons collide with the electron at the 4-dimension vector of  $(x_1, 0, 0, t_1)$  and  $(x_2, 0, 0, t_2)$ . According to the Lorentz transformation between inertial frames:

$$\left\{ \begin{array}{l} x = \gamma(x' + \beta ct') \\ y = y' \\ z = z' \\ t = \gamma\left(t' + \frac{\beta x'}{c}\right) \end{array} \right. \quad (1.20)$$

and because we set  $x' = 0$ , from Equation 1.20, the two events of two successive photons collide with the electron can be expressed as:  $(\gamma v t'_1, 0, 0, \gamma t'_1)$  and  $(\gamma v t'_2, 0, 0, \gamma t'_2)$ . As Figure 1.5 shows, the time interval of two successive photons (reciprocal of frequency) in frame  $S$  is:

$$\begin{aligned} \Delta t &= (t_2 - t_1) + \frac{(x_2 - x_1) \cos \theta}{c} \\ &= \gamma(t'_2 - t'_1) + \frac{\gamma v (t'_2 - t'_1) \cos \theta}{c} \\ &= \Delta t' \gamma (1 + \beta \cos \theta) \end{aligned} \quad (1.21)$$

Equation 1.21 shows that the relationship of photon number density between frame  $S$  and  $S'$  is:

$$n' = n \gamma (1 + \beta \cos \theta) \quad (1.22)$$

Combine Eqs. 1.22 and 1.19 we can transfer the incident photon energy density from frame  $S$  to  $S'$  according to Equation 1.23

$$U'_{rad} = U_{rad} [\gamma (1 + \beta \cos \theta)]^2 \quad (1.23)$$

In Equation 1.23, the incoming photon energy density is a function of the incident angle ( $\theta$ ), in order to get the total photon energy density, we integrate

the equation over  $\theta$ . Then we get:

$$U'_{rad} = \frac{4}{3}U_{rad} \left( \gamma^2 - \frac{1}{4} \right) \quad (1.24)$$

Combine Eqs. 1.24 and 1.17, the total scattered radiation power is:

$$\begin{aligned} P' &= P \\ &= \frac{4}{3}\sigma_T c U_{rad} \left( \gamma^2 - \frac{1}{4} \right) \end{aligned} \quad (1.25)$$

As mentioned before,  $P'$  and  $P$  are the total radiation powers after scattering.

Before the low energy gain photons, they give away some energy first which is  $\sigma_T c U_{rad}$ . Therefore, we have to subtract this value from Equation 1.25 to calculate the rate of net energy gain, which is described by Equation 1.26.

$$\begin{aligned} P' = P = \frac{dE}{dt} &= \frac{4}{3}\sigma_T c U_{rad} \left( \gamma^2 - \frac{1}{4} \right) - \sigma_T c U_{rad} \\ &= \frac{4}{3}\sigma_T c U_{rad} \beta^2 \gamma^2 \end{aligned} \quad (1.26)$$

If we compare Equation 1.26 with Equation 1.11, we find that the form is very similar between these two equations.

$$\frac{P_{IC}}{P_{sync}} = \frac{U_{rad}}{U_B} \quad (1.27)$$

where  $U_B$  is the energy density of environment magnetic field.

#### 1.2.4 Curvature Radiation

Curvature radiation is the main source of gamma-ray photons. Charged particles not only move around magnetic field lines (synchrotron radiation), but

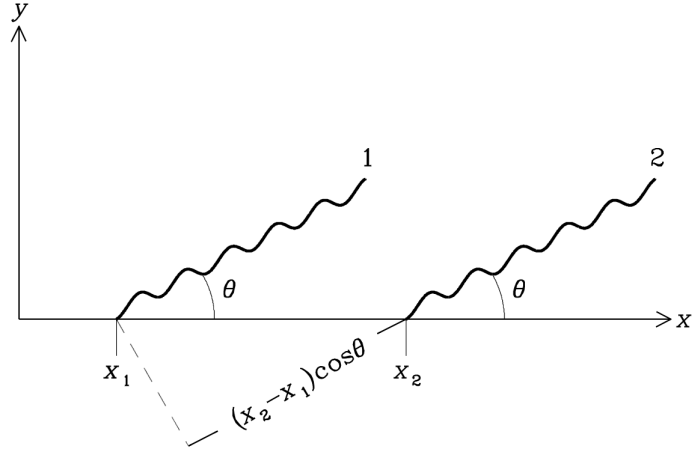


Figure 1.5: Two photons collide with an electron. In the frame  $S'$ , two photons collide with a rest electron successively. In the frame  $S$ , the electron is no longer at rest and the positions of the two events are  $x_1$  and  $x_2$

also along magnetic field lines (curvature radiation) because the magnetic field is very strong.

Equation 1.1 shows that total synchrotron radiation power is related to pitch angle (because of the term  $B_\perp$ ), and if the pitch angle is 0, there will be no synchrotron radiation. However, curvature radiation can still be generated and is dependent on the curvature radii of magnetic field lines:

$$P = \frac{2}{3} \frac{e^2 c}{s^2} \gamma^4 \quad (1.28)$$

where  $s$  is the curvature radii of magnetic field lines. Equation 1.28 is very similar to the Equation 1.2 and the only difference is that  $R$  is changed to  $s$ . Similarly, according to the Equation 1.3, the power spectrum of curvature radiation can be written as:

$$P = \frac{\sqrt{3} e^2}{m_e s} \gamma \left( \frac{\nu}{\nu_c} \right) \int_{\nu/\nu_c}^{\infty} K_{5/3}(\eta) d\eta \quad (1.29)$$

where  $\nu_c$  is the critical frequencies of curvature photons and equals to:

$$\nu_c = \frac{3}{4\pi} \frac{c}{s} \gamma^3 \quad (1.30)$$

According to Eqs. 1.28, 1.29 and 1.30, the spectral properties of curvature radiation are similar to synchrotron radiation. The only differences in the equations are particles' Lorentz factors and curvature radii.

## 1.3 Millisecond Pulsar

### 1.3.1 $P\text{-}\dot{P}$ Diagram

$P\text{-}\dot{P}$  diagram is an important tool for analyzing evolutions of pulsars. Period ( $P$ ) and time derivative of period ( $\dot{P}$ ) are two of pulsars' important characteristics. Analyzing the position of a pulsar in the  $P\text{-}\dot{P}$  diagram can give us some valuable information such as which evolution stage the pulsar is in or the type of the pulsar, etc. Figure 1.6 is an example of a  $P\text{-}\dot{P}$  diagram. The horizontal axis is pulsars' rotation periods and the vertical axis is time derivative of rotation periods ( $\dot{P}$ ). In this  $P\text{-}\dot{P}$  diagram, the negative slope lines represent the strengths of surface magnetic fields while the positive slope lines represent the characteristic ages of pulsars. The following is a short explanation for this. From previous discussion, we have known that the characteristic age of a pulsar is  $\tau = -P/\dot{P} = P/(-\dot{P})$ , so line of constant  $\tau$  is a set of straight lines with equal positive slope. We also know  $B \propto \sqrt{P\dot{P}}$ , therefore the line of constant  $B$  should be a part of hyperbola. However, a  $P\text{-}\dot{P}$  diagram is usually in log-log scale. Hence, if we let  $P' = \log P$  and  $\dot{P}' = \log \dot{P}$ ,  $B \propto \sqrt{P\dot{P}}$  turns to  $B \propto 1/2(P' + \dot{P}')$ , which represents a straight line.

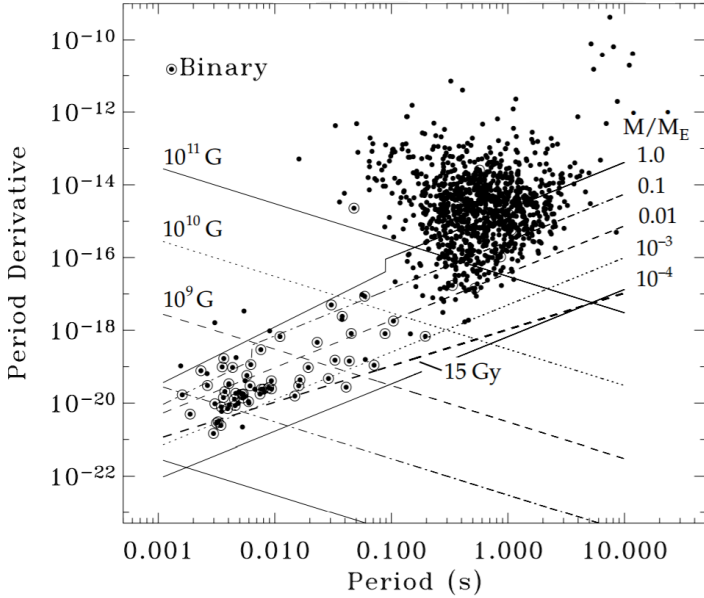


Figure 1.6: Position of pulsars in  $P-\dot{P}$  diagram

Figure 1.6 shows that most pulsars lie in the position of about 1s,  $10^{-14}\text{s/s}$ .

At the same time, a couple of stars lie at the bottom-left of Figure 1.6 — these are millisecond pulsars (MSPs). Their rotation periods are about 1-20 milliseconds. It is believed that MSPs are spun up by accretion of mass from their companion stars. In the above  $P-\dot{P}$  diagram, we can observe that millisecond pulsars' surface magnetic fields are about three to four orders of magnitude lower than those of normal pulsars. However, an MSP has a relatively strong magnetic field near its light cylinder. The reason is that an MSP's radius of light cylinder ( $R_{lc} = c/\omega$ ) is much smaller than a normal pulsar's because of its short rotation period and the magnetic field near light cylinder can be estimated as  $B_{lc} \sim (R/R_{lc})^3$ . At the same time, pulsars' emission mechanism is closely related to their magnetic field near the light cylinder. As a result, like a normal pulsar, an MSP also can have broadband spectrum from radio to gamma rays.

### 1.3.2 Origin Of Millisecond Pulsars

From pulsars' emission mechanisms, we know that magnetic field of a pulsar decreases with time while the spin period increase with time. But MSPs' spin periods are much shorter than normal pulsars and surface magnetic fields are a lot weaker. This makes an MSP seem to be both young and old. As a result, people think millisecond pulsars are old pulsars spun up by their companions. The companion stars transfer mass and angular momentum to accelerate the rotation speed of pulsar. Therefore, the aged pulsar can spin faster gradually.

### Mass Transfer And Accretion In Binary Systems

X-ray binaries are a type of binary systems that is luminous in X-ray band. There are several kinds of X-ray binaries including low mass X-ray binaries (LMXB) and high mass X-ray binaries (HMXB). The mechanism of transferring mass is different in these two types of systems. Before discussing mass transfer, we need to know a little bit about Roche Lobe. Figure 1.7 is a schematic diagram of Roche Lobe. We call two stars in an LMXB as A and

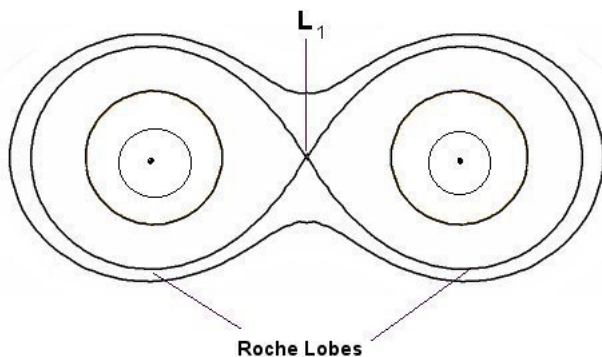


Figure 1.7: A schematic diagram of Roche lobe. $L_1$  is called inner Lagrange point which is the intersection of equipotential lines of star A and B.

B respectively for convenience. It is obvious that if an object is close to star

A, the gravitational influence of A is so strong that we can nearly ignore the effect of the star B. Similarly, this is true for star B. As a result, there must be a point where the effect of star A is equal to star B which is called inner Lagrange point [13]. The two parts inside the largest equipotential lines of A and B are called Roche lobe. If star B crosses its Roche lobe, than its mass will be attracted by A thus mass transfer between A and B happens. We should notice that this is the main way of mass transfer in LMXB. While in HMXB, the mass can be transferred by strong wind of the massive companion star.

What should be noted is that mass transfer can change the distance between two companion stars. If a low-mass star transfer mass to a high-mass companion star, the orbital separation will become larger. This can actually stop mass transfer and is a negative feedback. On the contrary, mass transfer from high-mass star to low-mass star will shrink the orbital distance.

### 1.3.3 Class II MSPs

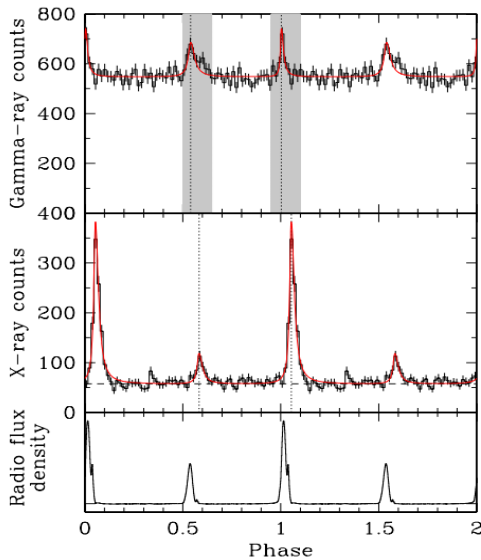


Figure 1.8: Pulse profiles of PSR B1937+21 in radio, X-ray and gamma-ray. [11]

Radio emissions are usually considered to be emitted above the polar cap, which means radio emissions and gamma-ray emissions are from different location of a pulsar's magnetosphere. However, there are about 10 sources showing aligned pulse profiles in radio and gamma-ray implying that radio emission may produced from outer magnetosphere and they are called Class II MSPs [7]. These pulsars have strong magnetic fields near the light cylinder. Figure 1.8 is an example of aligned pulse profile.

## 1.4 Previous Work and Objectives

The three energetic millisecond pulsars PSRs J0218+4232, B1821-24 and B1937+21 show broadband spectra across radio, X-ray and gamma-ray bands like young pulsars. Table 1.1 lists some basic information of the three MSPs. The three MSPs are some of the most energetic MSPs as the table shows. Some researches of gamma-ray spectra properties have been done using *Fermi Lat*. The spectra were fitted with the power-law-with-exponential-cutoff model (PLExpCutoff) and the results are shown in Table 1.2.

	J0218+4232	B1821-24	B1937+21
Period ( $ms$ )	2.32	1.56	3.05
Period Derivative ( $\dot{P} 10^{-20} ms ms^{-1}$ )	7.74	10.5	162
Spin Down Age ( $10^8 yr$ )	4.76	29.9	2.35
Surface Magnetic Field ( $10^8 gauss$ )	4.29	22.5	4.09
Light Cylinder Magnetic Field ( $10^5 gauss$ )	3.21	7.40	10.2
Spin Down Energy ( $10^{35} \dot{E}, erg s^{-1}$ )	2.4	022	11.6

Table 1.1: A few intrinsic properties of PSRs J0218+4232, B1821-24 and B1937+21. The data is from ATNF Pulsar Catalogue. [12]

	J0218+4232	B1821-24	B1937+21
Energy Range (GeV)	$0.1 \sim 100$	$0.1 \sim 100$	$0.5 \sim 6$
Photon Index $\Gamma$	$2.0 \pm 0.1$	$1.6 \pm 0.3$	$1.43 \pm 0.87$
Cutoff Energy (Gev)	$4.6 \pm 1.2$	$3.3 \pm 1.5$	$1.15 \pm 0.74$
Photon Flux ( $10^{-8} \text{ cm}^{-2} \text{ s}^{-1}$ )	$7.7 \pm 0.7$	$1.5 \pm 0.6$	$1.22 \pm 0.23$
Energy Flux ( $10^{-11} \text{ erg cm}^{-2} \text{ s}^{-1}$ )	$4.56 \pm 0.24$	$1.3 \pm 0.2$	$1.98 \pm 0.32$

Table 1.2: A few intrinsic properties of PSRs J0218+4232, B1821-24 and B1937+21. [12] [11] [6]

In the paper [6], they only study the PSR B1937+21 with energy range from 0.1 GeV to 6 GeV and another paper [11] studied the MSP more thoroughly with a wider energy range. The paper proposed that a power-law model is preferred and the photon index is  $2.38 \pm 0.07$  with a TS value of 112.

These paper are a little bit old and now we have about 4-year more *LAT* data. Besides, in year 2015, Fermi team released Pass 8 data including many improvements, such as better energy measurement and significantly improved effective area. As a result, it is reasonable to redo the gamma-ray analysis with the newer dataset and more observation data in order to gain more reliable results.

Therefore, my main objective is to use the new data to redo the gamma-ray analysis of the three energetic MSPs mentioned above. Then, I will do a numerical simulation based on a theoretical model called two-lay model and test if the the predictions of the model are consistent with the new observation data. And finally, based on numerical simulations of the two-layer emission model, I will generate broadband spectra (including hard X-ray band and gamma-ray band) for all the three MSPs.

# Chapter 2

## Gamma-Ray Analysis

As mentioned before, because of very short rotation periods, MSPs usually have very small light cylinder compared with normal pulsars. As a result, their emission mechanisms are similar to normal pulsars, especially for my target objects — PSRs J0218+4232, B1937+21 and B1821-24, which are among the fastest spinning MSPs. Therefore, as normal pulsars, the three MSPs have broadband emissions so it is convenient to analyze the spectra properties of them in gamma-ray band.

### 2.1 Introduction to the *Fermi Gamma-ray Space Telescope*

The *Fermi Gamma-ray Space Telescope* was launched on June 11, 2008 and opened a new window of studying supermassive black-hole systems, pulsars and so on. Its original name was *Gamma-ray Large Area Space Telescope* (GLAST) and changed to *Fermi Gamma-ray Space Telescope* in honor of the great scientist Enrico Fermi.

The *Fermi Gamma-ray Space Telescope* contains two parts: *Gamma-ray Burst Monitor (GBM)* and *Large Area Telescope (LAT)* and the latter is the main instrument which is at least 30 times more sensitive than all gamma-ray telescopes launched before. I only use LAT for my purposes. Thus I focus on the LAT instrument, which contains four main subcomponents including trackers, calorimeters, an anti-coincidence detectors and data acquisition systems. The reason why the telescope is designed in this way is that high-energy gamma-rays cannot be refracted by lens or mirrors. Therefore, the working principals of the *Fermi Lat* and other gamma-ray telescopes are completely different.

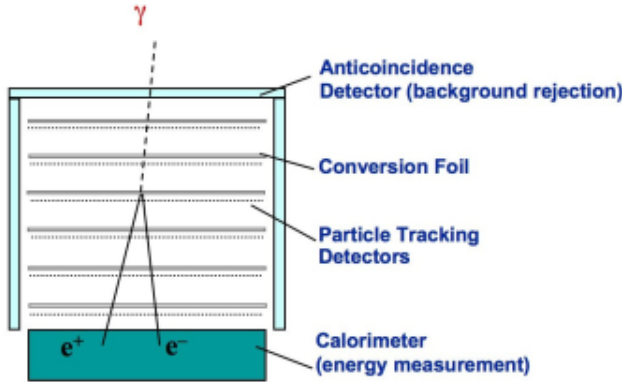


Figure 2.1: The figure ( <https://www-glast.stanford.edu/instrument.html> ) illustrates how *Fermi Lat* tracks incident gamma-ray photons.

Figure 2.1 demonstrates the very basic idea of the *Fermi Lat* working principles.

- Gamma-ray photons can enter the anti-coincidence detector freely while cosmic-rays will generate signals which then tell the data acquisition system component to reject these particles. In this way, the *Fermi Lat* can distinguish the gamma-ray photons from high energy cosmic-rays with a confidence level over 99.9%.
- The conversion foil (Figure 2.1) can convert gamma-ray photons into

electron and positron pairs. This procedure makes it possible to determine the directions of the incident gamma-ray photons.

- The tracker (particle tracking detectors in Figure 2.1) records the positions of the electrons and positrons generated from the gamma-ray photons. There are many trackers so the paths of a particles can be constructed by doing numerical simulations.
- When the electrons and positrons reach the calorimeter, their energies can be measured. By calculating the energy relationships between the gamma-ray photons and the corresponding electrons and positrons, the energies of the original gamma-ray photons can also be obtained.
- The data acquisition system is like a filter of gamma-ray photons which can reject unwanted particles such as cosmic-rays. Also, photons come from the Earth’s atmosphere are also rejected.

For a telescope, the ability of measuring the directions and energies of incident photons is very crucial. From the above descriptions of the *Fermi Lat* working principles, we know that the precision of construction of particles’ paths heavily influences how well we can measure the directions and energies of gamma-ray photons. And this process is greatly dependent on simulations and available Fermi datasets, , which means that with the improvements of simulations and datasets, the precision and sensitivity of *Fermi Lat* can also be improved. The Pass 8 data have reprocessed the entire Fermi mission dataset so the quality of the dataset is much better. This is part of the reason why I redo the analysis of the three MSPs.

## 2.2 A Brief Introduction to Fermi Data Analysis

### Processes of Doing Fermi Analysis

When doing *Fermi Lat* data analysis, I basically dealt with two parts. The first part is processing observation data and the second is generating photon distributions based on models. Cleaning data is straightforward including data selection, data filtering with good time intervals (GTIs), generating count maps and so on. Generating model-based count maps and count cubes needs a little bit more efforts and mainly includes the following procedures.

Firstly, I need to generate a spectra model of all sources in our region of interest (ROI). The model basically describes how strong each source is in different energy bands and different positions. The initial parameters of the model are from Fermi database. I do not fit positions of both point sources and diffuse sources when do the data analysis. However, the model alone is not very helpful and I have to know other informations in order to simulate photon distributions.

Since I am going to compare my simulation with the observation data, I have to take the telescope states into account. For example, the effective area of telescope decreases when away from the optical axis. In addition, inclination angles and observation time intervals have direct influences on the number of photon counts. In short, after I get the simulated photon distribution from a model, it is necessary to transfer the initial simulation into the real simulation by applying the telescope functions.

After obtaining the photon distributions and spectra simulations, I then can do comparisons in order to get the maximum likelihood of the model. I divide the total energy band into many smaller energy bins and denote the number of photon counts in observation data as  $n_i$ , so that  $\sum_i n_i = N$ , where  $N$  is the total number of photons in full energy range. The observed number of photon counts in  $i$ th bin is a Poisson distribution with a mean of  $m_i$ . In fact, the value  $m_i$  is the expected number of photon counts from our spectra model. Therefore, the distribution for  $i$ th bin can be expressed by Equation 2.1, where  $P_i(n_i)$  is the possibility of observing the  $n_i$  photon counts for the  $i$ th bin.

$$P_i(n_i) = \frac{e^{-m_i} m_i^{n_i}}{n_i!} \quad (2.1)$$

As a result, it is not hard to generalize the possibility for each bin to all bins, just by multiplying the possibilities for different bins.

$$\begin{aligned} P_{total} &= \prod_i P_i(n_i) \\ &= e^{-\sum_i m_i} \prod_i \frac{m_i^{n_i}}{n_i!} \end{aligned} \quad (2.2)$$

In Equation 2.2,  $n_i$  is directly from observation data so they usually can not be changed during the binned likelihood analysis. However, by changing the model, the  $m_i$  can be altered. Hence, my aim is to tweak the spectra model in order to make the total possibility  $P_{total}$  as large as possible.

This is the basic idea and procedure of doing Fermi data analysis. After doing these, we can go further such as testing how significant our targets are by creating TS maps. The thesis basically follows the procedures.

Before finishing this part, I should briefly introduce the basic idea of TS maps. TS value stands for Test Statistic value which can be expressed as Equation 2.3

$$TS = -2 \ln \frac{L_{max,0}}{L_{max,1}} \quad (2.3)$$

where  $L_{max,0}$  and  $L_{max,1}$  are the maximum likelihood of models in which the target source is not included and included respectively. According to Equation 2.3, the larger the TS value is, the larger  $L_{max,1}$  is, which means that the probability of existence of the target source is larger. In order to generate a TS map, I divide the whole map into many sub-grids. In each sub-grid, the “gtlike” algorithm basically does two things. The first procedure is calculating the maximum likelihood value directly based on the spectra model ( $L_{max,0}$ ). Then it adds an imaginary source in the sub-grid, fits the source and gets the maximum likelihood ( $L_{max,1}$ ) value. Therefore, we have two maximum likelihood values. In the end, it calculate the TS value for the sub-grid according to Equation 2.3.

After having the TS values for all sub-grids, we can generate a TS map just by rendering colors according to each grid’s TS value. By comparing TS values of all sub-grids in a TS map, I can determine where the target source is most likely to be and how large the probability is.

Generally speaking, for each source, I generate two TS maps and determine how likely my target source is observed. For instance, if the data show the source is observed, then the value of each pixel of the TS map containing the source should be low. On the contrary, the TS values of the pixels around the position of the target source should be significantly higher than other positions in the TS map if the target source is deleted from the model.

## 2.3 *Fermi Lat* Data Analysis

The basic idea of fitting spectra parameters is to make the count cube generated by the model be as similar to the observation data as possible. A count cube is just a combination of many count maps in different energy bands. For example, a dataset whose energy range is from 100MeV to 100GeV can be divided into 30 bins. We can generate a count map in each energy bin, thus we have 30 count maps.

A count map is basically generated by the following steps. Firstly, we choose a pixel with a certain size. Then we check each photon's direction to determine if the photon is in this pixel. If it is in the pixel, the photon counts of the pixel will add one. Therefore the more photons fall within the pixel, the more photon counts the pixel has, hence the brighter the pixel is. By doing the same thing for every pixel in the ROI, a count map can be generated. A count map tells us know what we have observed intuitively and offers a very basic idea of if the desired data is processed.

The calculation process can be summarized as follows. First of all, we have to generate a spectral model for every source in the region of interest (ROI) based on the Fermi database. The database includes *LAT* four-year Point Source Catalog (3FGL), Galactic diffuse emission (gll\_iem\_v06.fits) and isotropic emission (iso\_P8R2\_SOURCE\_V6\_v06.txt). Then we can produce a count cube based on the model. Generally speaking, the difference of the count cubes between the model and observation is obvious. Then, the Fermi software adjusts the parameters to make the difference smaller. Until the errors are acceptable, the software outputs the final fitted parameters of corresponding spectral models.

I use a power-law with exponential-cutoff (PLExpCutoff) model to fit the observation data and it is a special case of the power-law with super-exponential-cutoff (PLSuperExpCutoff) model. The spectra of PLSuperExp-Cutoff can be described by Equation 2.4:

$$\frac{dN}{dE} = N_0 \left( \frac{E}{E_0} \right)^{\gamma_1} \exp \left[ - \left( \frac{E}{E_c} \right)^{\gamma_2} \right] \quad (2.4)$$

where  $N_0$  is called prefactor,  $E_c$  is the cutoff energy and the  $E_0$  is a scale parameter. PLExpCutoff model is the special case where  $\gamma_2 = 1$ . My aim is to fit the parameters  $N_0$ ,  $E_c$  and  $\gamma_1$  to make the model be more consistent with the *Fermi Lat* observation data.

### 2.3.1 Verifying the Data Analysis Process

Before analyzing the observations of my target sources, it is reasonable to test if my procedures of data processing are right. In order to do so, I try to do analysis for two bright pulsars PSRs J0007+7303 and J0534+2200. The reason I choose these two pulsars is that according to previous studies, they are bright and easy to detect with a large TS value of 43388 and 102653 for J0007+7303 and J0534+2200 respectively. [2]

In the spectra fit process, I do not use the same fit parameters as the previous paper, (for instance, the number of free parameters in the ROI is different) however, I get similar results in terms of spectra index. In Table 2.1, I used the observation data from 2009-01-01 to 2013-02-01 in order to try to be consistent with the old paper [2]. In addition, I also fit spectra with observation data up to 2018-02-01 and *Pass 8 dataset* to test how big improvement I can make with the new *Fermi Pass 8* dataset and more observation data. The results of year 2018 data are shown in Table 2.2.

Tables 2.1 and 2.2 mainly show two pieces of information. Firstly, my procedures of dealing with observation data has no obvious problems, so basically I can trust fit results of my target sources. Secondly, the *Fermi Pass 8 Lat Data* has improved the accuracy a lot. For example, as Table 2.1 shows, the photon indexes are  $1.30 \pm 0.02$  and  $1.4 \pm 0.1$ , which shows that the errors reduce a lot. Additionally, the TS value is more than double as before. <question>However, the cutoff energies are not consistent between the previous result and the new result. (I need to explain this a little bit later).</question>

	Test Results			Previous Results		
	$\Gamma$	$E_c$ (MeV)	TS	$\Gamma$	$E_c$ (MeV)	TS
J0007+7303	$1.30 \pm 0.02$	$2010 \pm 85$	96979	$1.4 \pm 0.1$	$4700 \pm 200$	43388
J0534+2200	$2.07 \pm 0.01$	$9880 \pm 572$	239015	$1.9 \pm 0.1$	$4200 \pm 200$	102653

Table 2.1: The spectra fit results. In the thesis, in order to make data analysis more convenient, I use some pipeline scripts to deal with the observation data. The "Test Results" column is the results generated by using the pipeline scripts. The "Previous Results" column lists the corresponding spectra properties based on the previous studies [2]. According to the standard PLExpCutoff model (described in equation 2.4,  $\Gamma$  is photon index and  $E_c$  is cutoff energy.)

$\Gamma$	$E_c$ (GeV)	TS value
J0007+7303	$1.34 \pm 0.02$	$2.20 \pm 0.67$
J0534+2200	$2.01 \pm 0.01$	$9.20 \pm 0.37$
		210166
		449946

Table 2.2: Fit results with data from year 2009 to year 2018. The physical meanings of  $\Gamma$  and  $E_c$  are the same as Table 2.1

## 2.4 PSR J0218+4232

The ROI is a circle with radius of  $20^\circ$  and all parameters of sources which are  $8^\circ$  outside of the center are fixed. For sources within  $8^\circ$ , initial values of parameters are the same as their default values according to *Fermi Lat four-year Point Source Catalog*. In this case, there are seven point sources which have free parameters. In Figure 2.2, the green circles represent those sources. There are some very bright sources which have no free parameters in the outer parts of the count map. The reason is that they are so far away from PSR J0218+4232 that *Fermi Lat* can distinguish if a photon comes from the target source or outer sources. As a result, I do not need to fit any parameters for those outer sources and their spectra properties are from *Fermi Lat four-year Point Source Catalog*. However, it is different for the nearby sources and they have to be fitted.

### 2.4.1 Count Maps And Count Cubes

The left part of Figure 2.2 is the count map of PSR J0218+4232. In the center of the left panel, we can clearly see the target source. The dimensions of the figures seems to be weird and the reason why the count map is 141 pixels wide is that I need to select a circle region from the original data. However, when generating a count map, I have to assign the sizes for x and y axis separately, which means that the a count map is actually rectangular. As a result, I have to crop a rectangular from the original circle region and in this case, the rectangular is chosen as a square.

Figure 2.3 is a comparison between PSR J0218+4232's count maps in different energy bands. The count map in about 100MeV is so messy that we

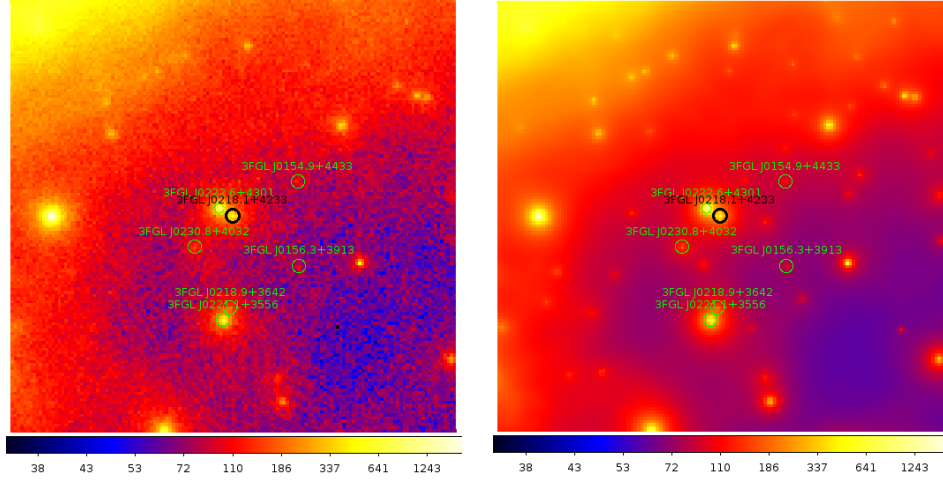


Figure 2.2: The count map of PSR J0218+4232 (left) and the count map generated by the model (right). In the left panel, the green circles represent sources needed to be fitted. The right panel is a count map created according to the fitted spectra model. The size of each figure is 141 pixels  $\times$  141 pixels, and the dimension for each pixel is  $0.2^\circ \times 0.2^\circ$ .

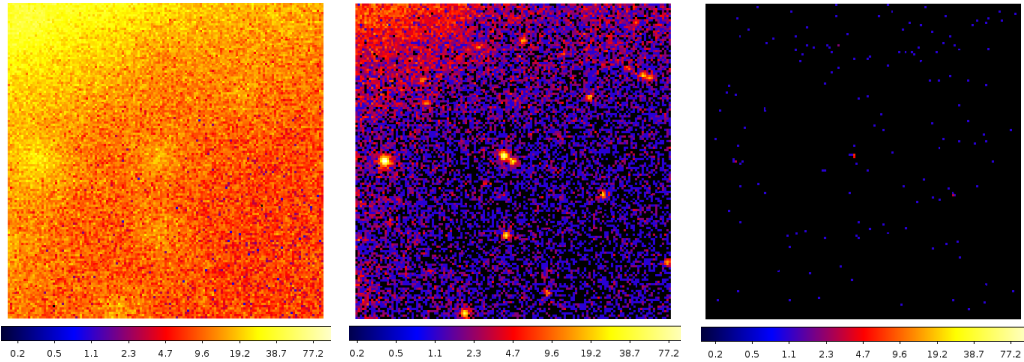


Figure 2.3: Three count maps from PSR J0218+4232's count cube. The energy ranges of the figures are 100~123MeV, 1.873~2.310GeV, 35.11~43.29GeV respectively.

can hardly distinguish the target source while the energy is above 30GeV there are so few photons that there is not a clear sign of the source. I choose three circle regions whose centers are the target sources and the radii are 1000 " for all of the three figures and then calculate the total numbers of photon counts of the selected regions. As Table 2.3 shows, though total number of photon counts around the target source is similar between the left and middle count

maps, the numbers of counts per energy are much different. Since there are few photons in high energy bands (above 50GeV) compare to other energy bands, I focus more on the lower energy part.

	Left	Middle	Right
Total counts	78	93	0
Energy range ( $MeV$ )	100~123	1873~2310	35110~43290
Counts / $MeV^{-1}$	3.39	0.21	0.00

Table 2.3: Numbers of photon counts of count maps in different energy bands for PSR J0218+4232.

### 2.4.2 Binned Likelihood Analysis

Figure 2.2 shows that the fit results of the model are consistent with the observation. However, there are lots of small red pixels in the left panel (generated directly by the observation data) while the right panel is very "clean". This means that a lot of photons are thought as generated by the modeled source. Thus in the model, the sources are generally slightly brighter than the observation. However, the target source is an exception. In the region I have used before (the center is the target source, and the radius is 1000''), the total photon counts in the left panel are 1815 compare to 1737 in the right panel.

The reason why the count map generated directly by the observation data is a lot more messy is that the source model is generated based on the Fermi database and their spatial position is fixed. This means that if a photon comes from a particular direction and there is no any known pulsar in that direction, this photon has to be classified into other directions and there is a modeled source in the direction. Thus, the spatial positions of photons are different between the observation and the model, and the count maps generated directly

from models are usually cleaner.

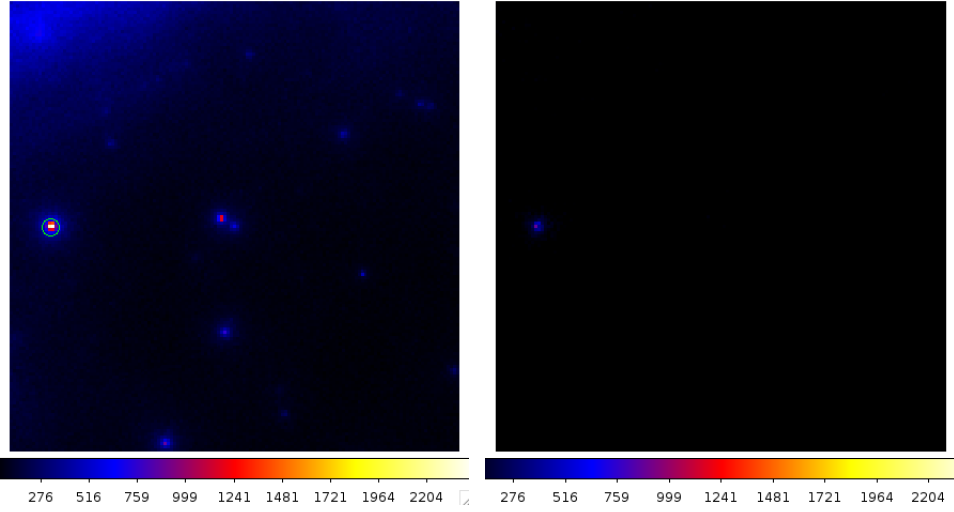


Figure 2.4: The count map and residual map of PSR J0218+4232. The figures are both in linear scale in order to compare the residual map between the original count map more intuitively. The left panel is the count map and the right panel is the residual map which shows the differences between the observation and the spectral model. It is created by directly subtracting the photon counts of each pixel between the count maps of observation data and the spectral model. The green circle region represents (the regions are completely the same in the two figures) the largest number photon counts of the residual map and its radius is 2000".

Figure 2.4 basically describes how well the model is compared to the observation data. There are some black dots and bright dots in the residual map showing the differences between the spectral model and the observation data. In the residual map of Figure 2.4, most differences of absolute photon counts are small, however, in the green circle region, the absolute value 6003 is large. This means that in this region, the number of photon counts of the observation data (21525) is 6003 larger than in our model. This is not negligible since it is nearly 28% of the original photon counts. Does this mean that the model is not good? The answer should be yes, however, this does not mean the fit is not good since the model parameters in this region are all fixed and the fixed values are from the Fermi Lat 4-year Point Source Catalog. Hence, the difference shows some problems of the spectral model, but has nothing to do

with the fit results. Instead, from the residual map, we can see that the fit results are good because the differences of number of photon counts are very low, which are about 5% of the photon counts of the count map on average.

Table 2.4 lists the results of the fit parameters. We see from Table 2.4 that the new fit results are consistent with the old ones. However, the precision improves a lot which is ascribed to the *Fermi Lat Third Source Catalogue* and *PASS 8* data. Figure 2.5 is a plot of the spectrum according to Function 2.4. One thing should be noticed is that we need to multiply  $E^2$  to Function 2.4 fit is consistent with flux points fitted by each energy bin separately. The TS value of our target source is 7110, which gives us a significance level  $\sigma \approx \sqrt{TS} = 84$ . This strongly implies the presence of our target source. We can also use a TS map to test the presence of the source as Figure 2.6 shows.

	This Study	Previous Results
Index1 ( $\gamma_1$ )	$1.89 \pm 0.04$	$2.0 \pm 0.1$
Cutoff ( $E_c$ , GeV)	$3.77 \pm 0.40$	$4.6 \pm 1.2$
Photon Flux ( $10^{-8} \text{ cm}^{-2}\text{s}^{-1}$ )	$7.29 \pm 0.28$	$7.7 \pm 0.7$
Energy Flux ( $1 \times 10^{-11} \text{ erg cm}^{-2}\text{s}^{-1}$ )	$4.45 \pm 0.16$	$4.56 \pm 0.24$
TS value	6809	1313

Table 2.4: Fit parameters of the spectral model of PSR J0218+4232. The names of parameters are consistent with Equation 2.4. The previous results are from the paper [2].

We can also check the count residuals of the fit as Figure 2.7 shows. The galactic and isotropic emissions are very bright compared with the target source and this can bring some difficulties to the fit (especially for the other two MSPs PSRs B1937+21 and B1821-24). The residuals and fluctuations become larger and more obvious when the energy is larger than 100MeV. Meanwhile,

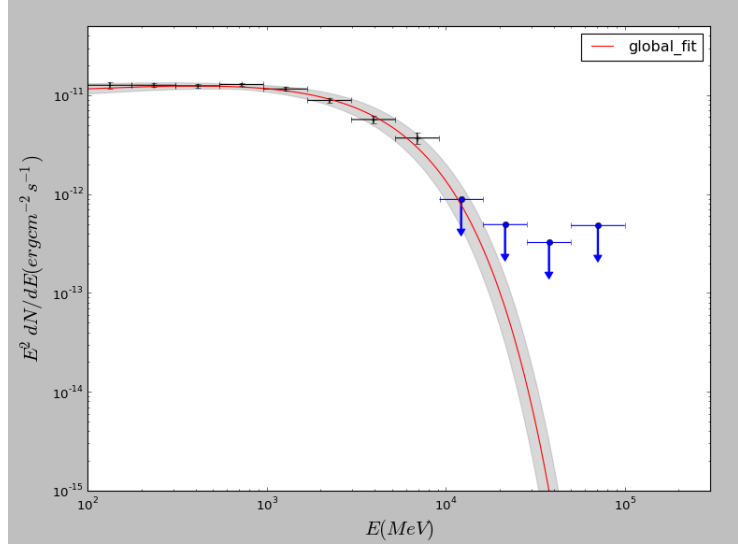


Figure 2.5: The log-log plot of flux to energy of PSR J0218+4232. The grey shade represents fitting errors, black points with error bars are flux points, the blue dots are upper values and the red line is the PLExpCutoff model multiplied by  $E^2$ . Flux points are fitted separately by dividing the total energy bin ( $100\text{ MeV} \sim 100\text{ GeV}$ ) into multiple energy bins. The horizontal error bars represents the width of each bin.

since the total number of counts in high energy bands is significantly smaller than in low energy bands, the error bars become much larger above 100MeV. At the same time, in low gamma-ray part (from 100MeV to 200MeV), the number of counts of the model deviates from observation counts obviously because of the relatively low energy resolution in low-energy gamma-ray part. The error of the first bin is larger than the next several bins in Figure 2.5 also shows that the fit in low-energy gamma-ray band (from 100MeV to 200MeV) is not as good as higher energy bands (but not too high).

## 2.5 PSR B1821-24

The ROI region is a circle whose radius is  $20^\circ$  and all parameters of sources outside of  $8^\circ$  are fixed. There are six free sources in the region of  $8^\circ$ . Figure 2.8 is a combination of count maps of observation data and the model.

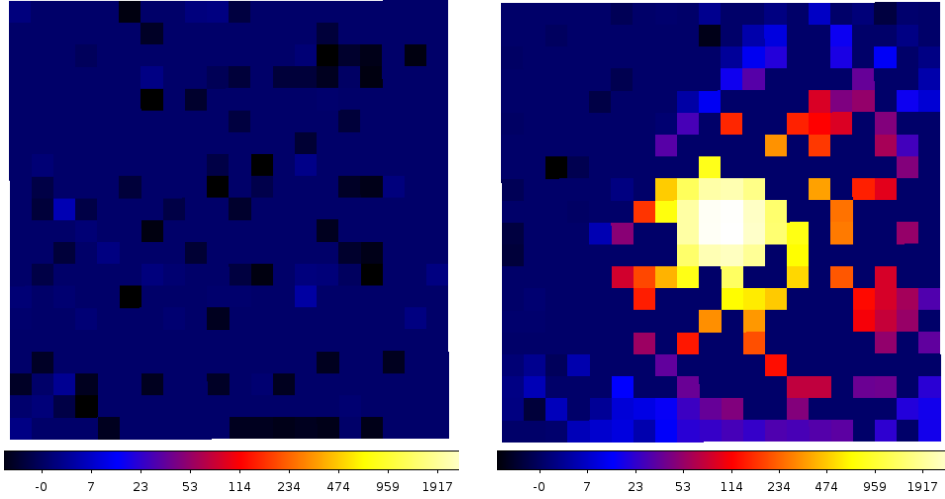


Figure 2.6: TS maps of PSR J0218+4232. The figures' dimensions are  $4^\circ \times 4^\circ$  (20 pixels  $\times$  20 pixels with  $0.2^\circ \times 0.2^\circ$  for each pixel). The left and the right panels are generated by the xml models with and without the target source PSR J0218+4232 respectively. The left panel shows that the possibility of adding an imputative point source is very low only with a maximum TS value of less than 5. However, the right panel strongly implies that there should be an additional source after I have removed the target MSP from the spectral model, which means it's highly likely that PSR J0218+4232 is contained in the observation data.

### 2.5.1 Count Maps And Count Cubes

The left and right panels of Figure 2.10 are the count map of the PSR B1821-24 generated from observation data and spectral model respectively. Like the situations of PSR J0218+4232, the count map from the model is clearly cleaner than from the observation data and the two figures are very similar, which implies that the spectra model describes the observation data well.

Figure 2.9 are count maps of PSR B1821-24 in different energy bands. The target pulsar is too faint in very high energy bands and interfered too much by the ambient environment in low energy bands (around 100MeV). PSR B1821-24 is near the M28 globular cluster and is the most energetic one, which is much brighter than other sources found in M28. However, since PSR B1821-

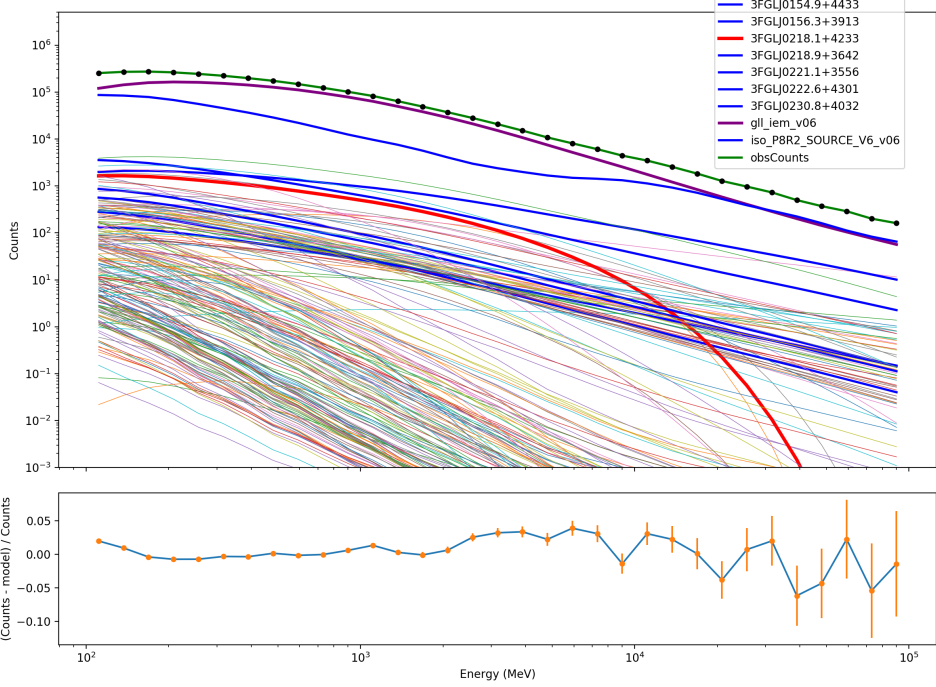


Figure 2.7: The count spectra and count residuals of PSR J0218+4232. The upper panel is the count spectrum of all sources included in the fit procedure. Thick lines are those sources with free fit parameters while the thin lines are fixed sources. The green line and the black dots represents observed counts in different energy bands. The purple line represents galactic emission. The lower panel shows the count residuals in different energy bands.

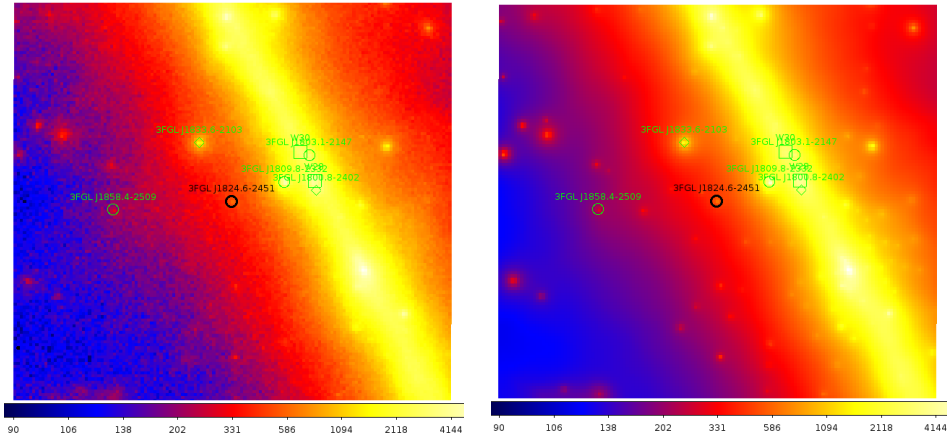


Figure 2.8: The count map of PSR B1821-24 (left) and the count map generated by the model (right). In the left panel, the green circles are free sources. The sizes of the both figures are 141 pixels  $\times$  141 pixels, and each pixel's dimension is  $0.2^\circ \times 0.2^\circ$ .

24 is very faint observed from Earth, it is reasonable that the fit result is not as good as the result of PSR J0218+4232.

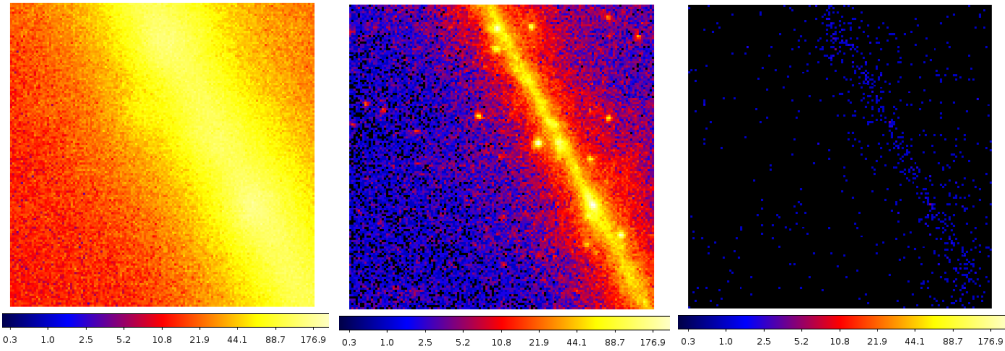


Figure 2.9: Three figures of PSR B1821-24's count cube. The energy ranges of the figures are 100~123MeV, 1.873~2.310GeV, 81.11~100GeV respectively from left to right.

### 2.5.2 Binned Likelihood Analysis

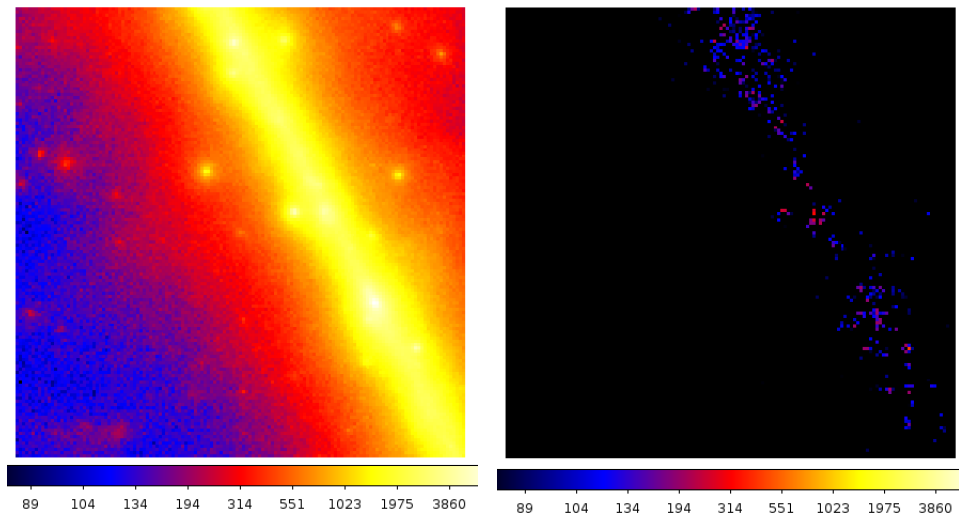


Figure 2.10: The count map and residual map of PSR B1821-24 in linear scale. The reason why use linear scale is not used here is that the residual map is nearly black in linear scale. The left figure is the count map and the right figure is the residual map showing the difference between the observation data and the spectral model.

The differences of the count map between the observation data and the model are described as Figure 2.10 which is in linear scale. In the right part of figure, there are some black dots with absolute values about  $-800$ . Though

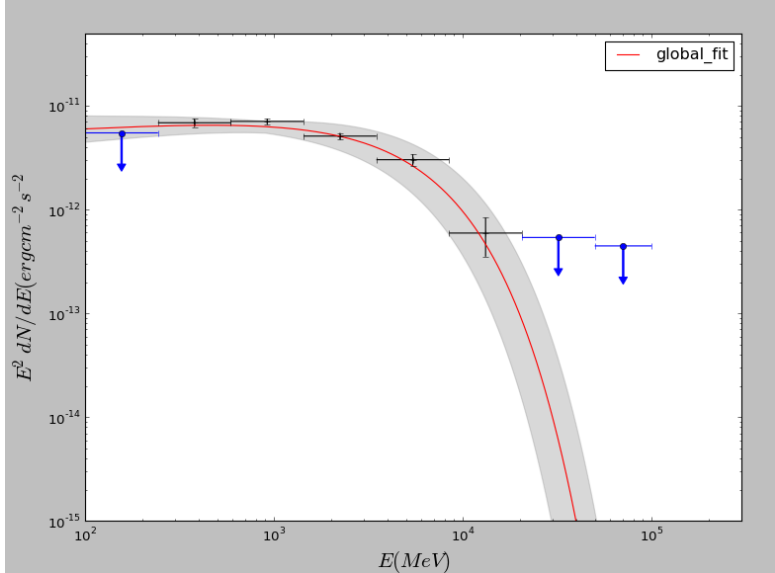


Figure 2.11: The log-log plot of flux to energy of PSR B1821-24's gamma-ray spectrum.

their values are relatively high, the number of high-value dots are very small so the fit is acceptable in general. But I am still trying to get the better spectra model.

Table 2.5 shows the global fit results of PSR B1821-24. The TS value of the model is 941 which gives us a significance level of about  $\sqrt{941} \sim 31$ . This strongly supports the existence of the target source in the observation data. As Table 2.5 shows, the energy flux from 100MeV to 100GeV is not consistent between the two studies and gamma-ray spectrum of the previous study is also softer [10].

Figure 3.3 shows that the global fit is consistent with the flux points generated by fitting sub-energy bins separately. We notice the upper value for the first energy bin is slightly smaller than the global fit. Though it is strange that the upper value is smaller than the normal value at first glance, it is reasonable since the flux points are fitted separately and are independent to the global fit. In fact, I use a single power-law model to fit each sub-energy bin while PLEExpCutoff model to do the global fit. As discussed previously, the

lower energy parts of the observation (around 100 MeV) is not as reliable as other energy bands. As a result, the separate fit for the first energy bin is not as good as the global fit and it is reasonable that the two fit results are not completely consistent. When this happening, I have more confidence on the global fit than the separate fit.

	This Study	Previous Results
Index1 ( $\gamma_1$ )	$1.91 \pm 0.07$	$1.6 \pm 0.3$
Cutoff ( $E_c$ , GeV)	$4.50 \pm 0.71$	$3.3 \pm 1.5$
Photon Flux ( $10^{-8} \text{ cm}^{-2} \text{s}^{-1}$ )	$3.85 \pm 0.31$	$1.5 \pm 0.6$
Energy Flux ( $10^{-11} \text{ erg cm}^{-2} \text{s}^{-1}$ )	$2.44 \pm 0.14$	$1.3 \pm 0.2$
TS value	941	76

Table 2.5: Fit parameters of the spectral model of PSR B1821-24. The names of parameters are also consistent with Equation 2.4. The energy ranges of photon flux between the two results are different.

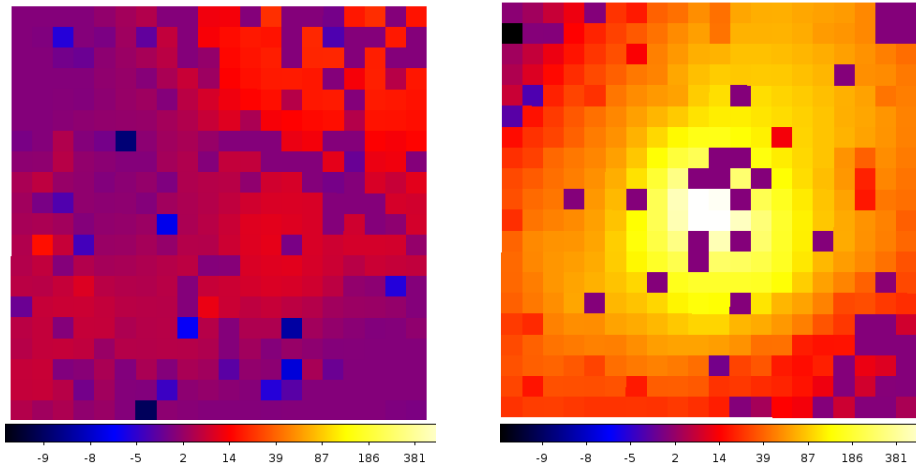


Figure 2.12: TS maps of PSR B1821-24. The figures' dimensions are  $4^\circ \times 4^\circ$  (20 pixels  $\times$  20 pixels with  $0.2^\circ \times 0.2^\circ$  for each pixel). The left and right panels are generated by the XML models with and without the target source PSR B1821-24 respectively. The left panel shows that the possibility of adding an imputative point source is very low only with a maximum TS value of less than 11 while the TS values of the right figure are generally much larger.

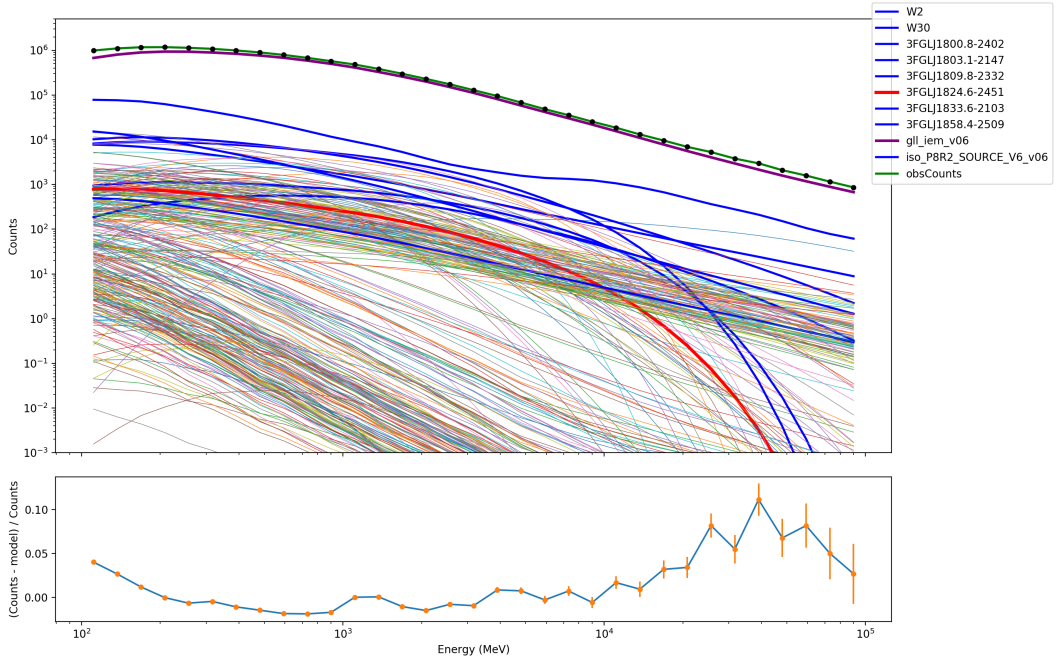


Figure 2.13: The count spectra and count residuals of PSR B1821-24A. The upper panel is the count spectrum of all sources included in the fit procedure. Thick lines are those sources with free fit parameters while the thin lines are fixed sources. The green line and the black dots represents observed counts in different energy bands. The purple line represents galactic emission. The lower panel shows the count residuals in different energy bands.

## 2.6 PSR B1937+21

### 2.6.1 Phase Averaged Analysis

First of all, I use a PLExpCutoff model to fit the gamma-ray spectra. In order to make the data analysis be more consistent, I choose the same parameters to process the raw observation data. Like the other two MSPs, the radius of the ROI is  $20^\circ$  degrees, and all parameters of sources  $8^\circ$  degrees outside from the center are fixed with default values. There are nine point sources including the target source PSR B1937+21 and twenty-eight free parameters. In fact, PSR B1937+21 is not included in *Fermi Lat four-year Point Source Catalog* may be because that the MSP is very weak and the signal to noise ratio is so low that we could not get reliable spectrum fit results with a large TS value. Thus I have to add the configuration file for the MSP manually and I set the initial value of photon index to be  $-2.5$ .

### Count Maps and Count Cubes

Figure 2.14 is the comparison of count maps between observation data. Like the previous conditions, the count map of observation data is more messy than the fitted model.

Figure 2.15 is the count maps in different energy bands. When energy is above about  $1.6\text{GeV}$ , there is very few photons. In many cases, people analyze spectra from  $100\text{MeV}$  to  $300\text{GeV}$  with *Fermi Lat*, however, the photon counts above  $100\text{GeV}$  is nearly negligible compared with the total counts. The total number of photon counts from  $100\text{MeV}$  to  $300\text{GeV}$  is about  $1.07 \times 10^7$  compared with 1175 from  $100\text{GeV}$  to  $300\text{GeV}$ . As a result, it is reasonable to use data

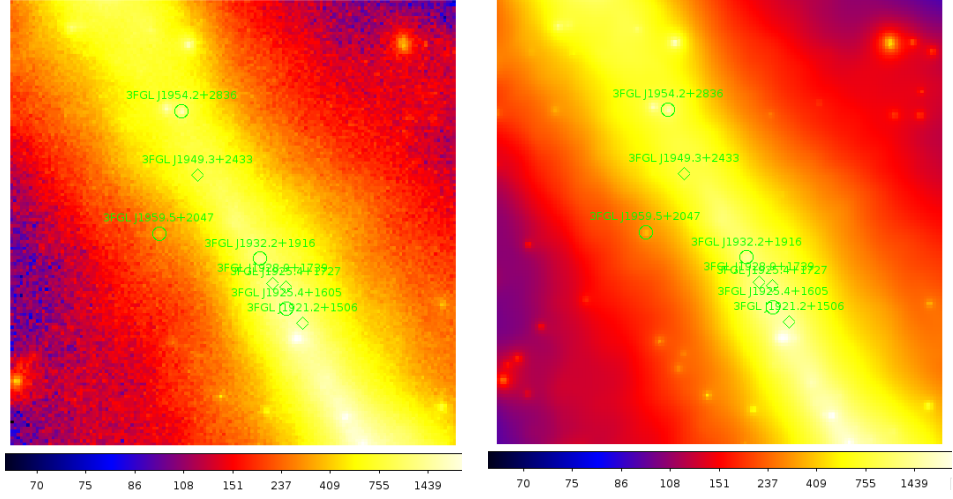


Figure 2.14: The count maps of PSR B1937+21 created from observation data (left) and from the spectral model (right). The dimensions of both figures are  $141\text{pixels} \times 141\text{pixels}$  and each pixel's size is  $0.2^\circ \times 0.2^\circ$ .

only from 100MeV to 100GeV. The case is also true for the other two pulsars — PSRs J0218+4232 and B1821-24.

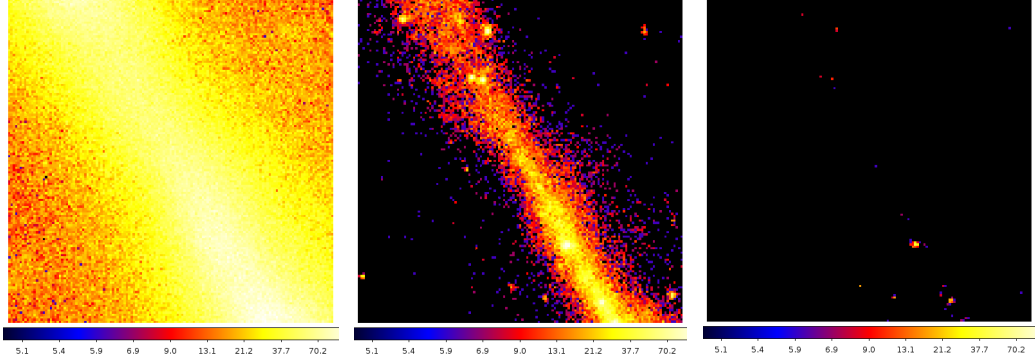


Figure 2.15: Three count maps of PSR B1937+21's count cube. The energy ranges of the figures are from 100 to 131 MeV, from 2460 to 3212 MeV, from 12198 to 15929 MeV respectively.

## Binned Likelihood Analysis

Figure 2.16 roughly describes how well the global fit is. Both left and right panel are in linear scale in order to make it easier to compare. As the residual map shows, there is no obvious difference between the fitted model and the

observation. The max value of the photon counts in the residual map is only about 270.

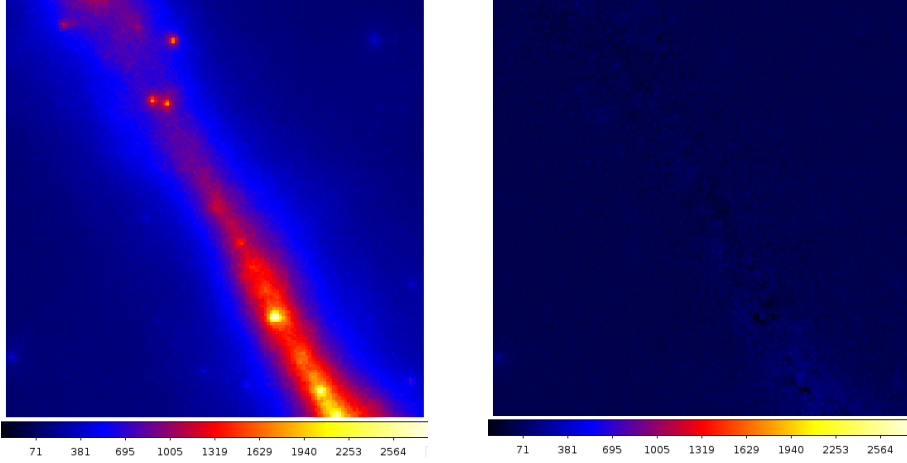


Figure 2.16: The count map created from observation data (left) and residual map (right) of PSR B1937+21. Both left and right panels are in linear scale. The dimension is  $141\text{pixels} \times 141\text{pixels}$  and each pixel's size is  $0.2^\circ \times 0.2^\circ$ .

Table 2.6 lists the fit results of PLExpCutoff model. According to the previous work [11], the PLExpCutoff model is not preferred over power-law model. Therefore, only the results of power-law model is reported in the paper. In this result, the PLExpCutoff model gives a TS value of 122, which is about the same as the previous results.

	This Study	Previous Results
Photon Index ( $\Gamma$ )	$2.61 \pm 0.22$	$2.1 \pm 0.2$
Cutoff Energy ( $E_c$ , GeV)	$4.90 \pm 2.29$	$8 \pm 4$

Table 2.6: Fit parameters of the spectral model of PSR B1937+21. The names of parameters are consistent with Equation 2.4. The old results are from the paper [11]. Note that since the paper prefers power-law model than PLExpCutoff model, it does not report the photon flux of PLExpCutoff model.

Figure 2.18 shows the residual counts of the global fit. The fit is good from 100MeV to about 20GeV. However, it goes significantly worse when energy is too high and the residual counts are much larger than the PSRs J0218+4232

and B1821-24.

Although the TS value for PSR B1937+21 is only 122, existence in gamma-ray of the target source is more obvious in the TS maps as the Figure 2.17 shows. Figure 2.21 contains the spectra shape of the PLExpCutoff model.

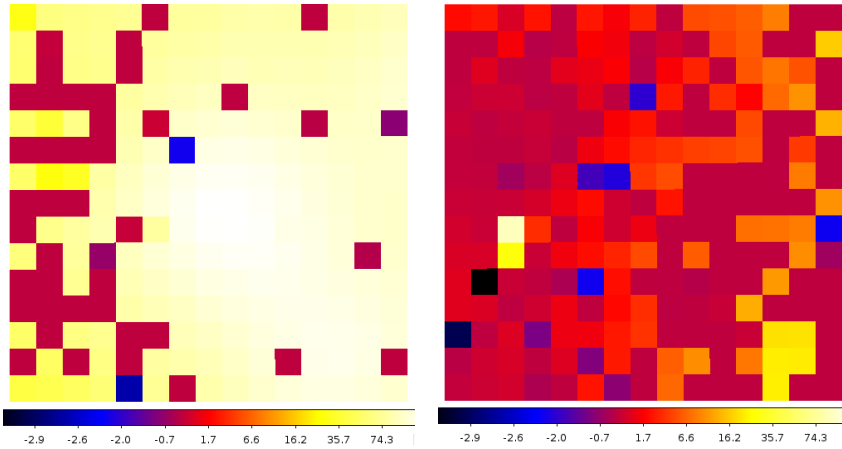


Figure 2.17: TS maps of PSR B1937+21. The dimension is  $3^\circ \times 3^\circ$  (15 pixels  $\times$  15 pixels and each pixel is  $0.2^\circ \times 0.2^\circ$ ). The left panel is generated by the model by removing PSR B1937+21 while the right panel contains the target source.

Since the fit results of PLExpCutoff model is not very satisfiable, I also fit the gamma-ray spectra with a power-law model. Because I have showed lots of count maps and they actually do not give us very much information, I do not show more count maps and count cubes for the analysis of power-law model. The photon index is  $2.94 \pm 0.13$  with a TS value of 147 as the Table 2.7 shows. Although the energy flux is consistent with the previous study [11], the photon index is not.

	This Thesis	Previous 1	Previous 2
Photon Index ( $\Gamma$ )	$2.94 \pm 0.13$	$2.38 \pm 0.07$	$3.02 \pm 0.18$
Energy Flux ( $10^{-11} \text{ ergcm}^{-2}s^{-1}$ )	$1.6 \pm 0.2$	$1.6 \pm 0.2$	

Table 2.7: Photon index comparison of power-law model between different studies. The data of column *Previous 1* is from the paper [11] and column *Previous 2* is from the paper [6].

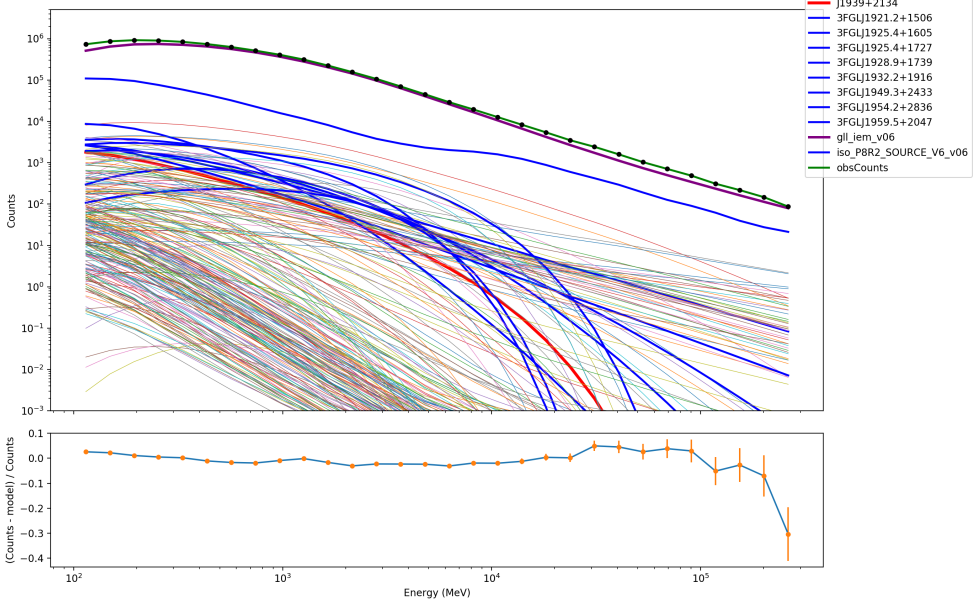


Figure 2.18: Top: count spectra for all sources included in the xml model (including sources with both free parameters and fixed parameters). Bottom: counts residual plot of the model. The thick red line is the target source PSR B1937+21, the blue thick lines are sources with free parameters and the thin lines are the sources with only fixed parameters.

Figure 2.19 is the count residuals of the fit and it is no better than Figure 2.18. But I also prefer a power-law model since the likelihood of the power-law model is much larger than the PLExpCutoff model. The Fermi tool *gtlike* gives a likelihood of the fitting model. We can compare the absolute value of the likelihood to know which model is preferred. The absolute value for power-law model is 18409504.4 compared with 4427799.496 for a PLExpCutoff model. And the spectrum of the power-law model is shown in Figure 2.21. Both power-law and PLExpCutoff models are consistent with the flux points, which are generated independently, and the flux points do not show a clear cutoff.

Figure 2.20 shows the TS maps with the target source and without the target source respectively.

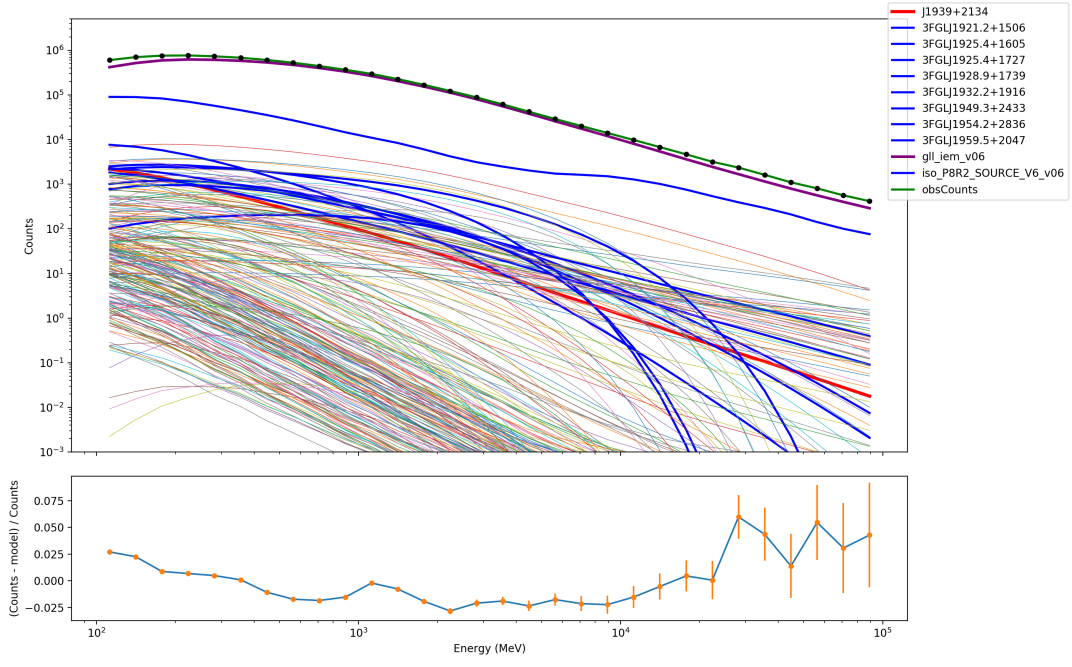


Figure 2.19: Top panel is counts spectra for all sources within the ROI. Bottom panel shows the counts residual.

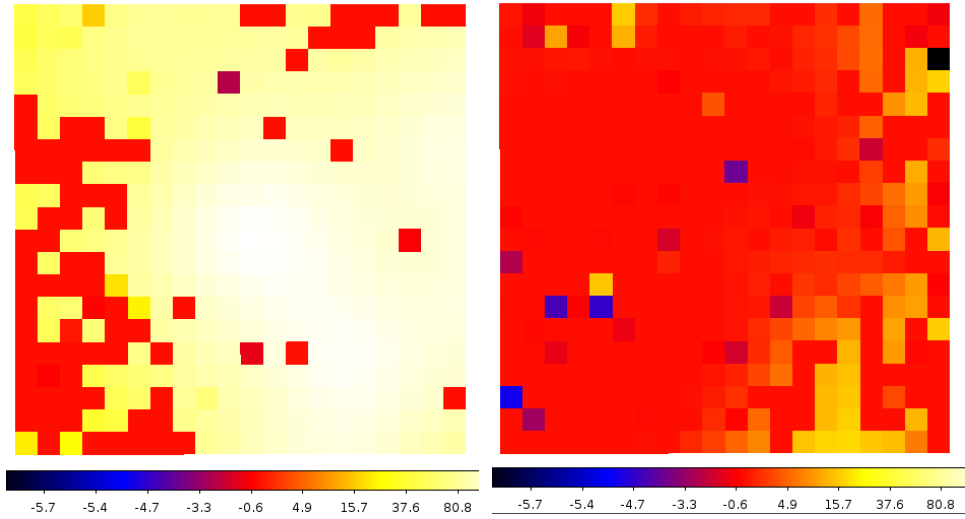


Figure 2.20: TS maps of PSR B1937+21 (power-law model). The dimension is  $4^\circ \times 4^\circ$  (20 pixels  $\times$  20 pixels and each pixel is  $0.2^\circ \times 0.2^\circ$ ). The left panel is generated by the model after removing PSR B1937+21 while the right panel contains the source.

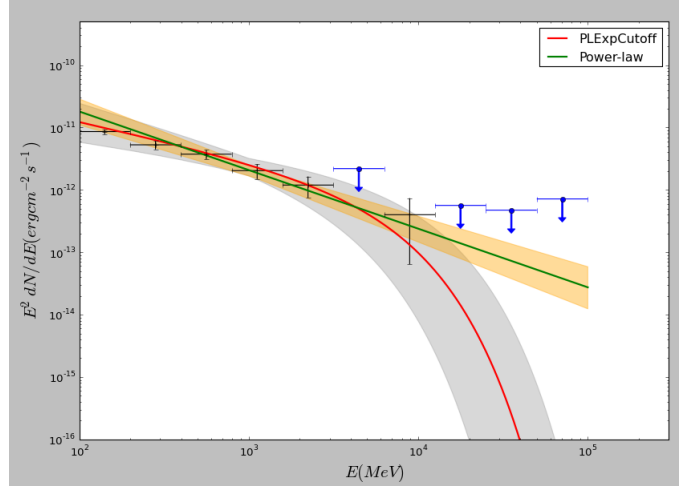


Figure 2.21: The log-log plot of flux to energy of PSR B1937+21’s gamma-ray spectrum. The red line represents the PLExpCutoff model and the green line is the power-law model.

## 2.6.2 Phase Resolved Analysis

Since the PLExpCutoff model is not a good model for phase-averaged spectrum of PSR B1937+21, I did a quick phase-resolved analysis for the MPS. I choose the phase of  $0.0 \sim 0.2$  and  $0.5 \sim 0.7$  from the full good time interval (GTI) as Figure 2.22 implies.

The light curve generated by *Fermi Lat* is consistent with the paper [6] as Figure 2.23 shows. The new light curve by *LAT* is better than the previous *LAT* light curve as shown in the figure.

The radius of the ROI is also set to  $20^\circ$  degrees, and all parameters of sources  $8^\circ$  degrees outside from the center are fixed with default values, which is the same as the above analysis. Figure 2.24 is the comparison of count maps between observation data and the model.

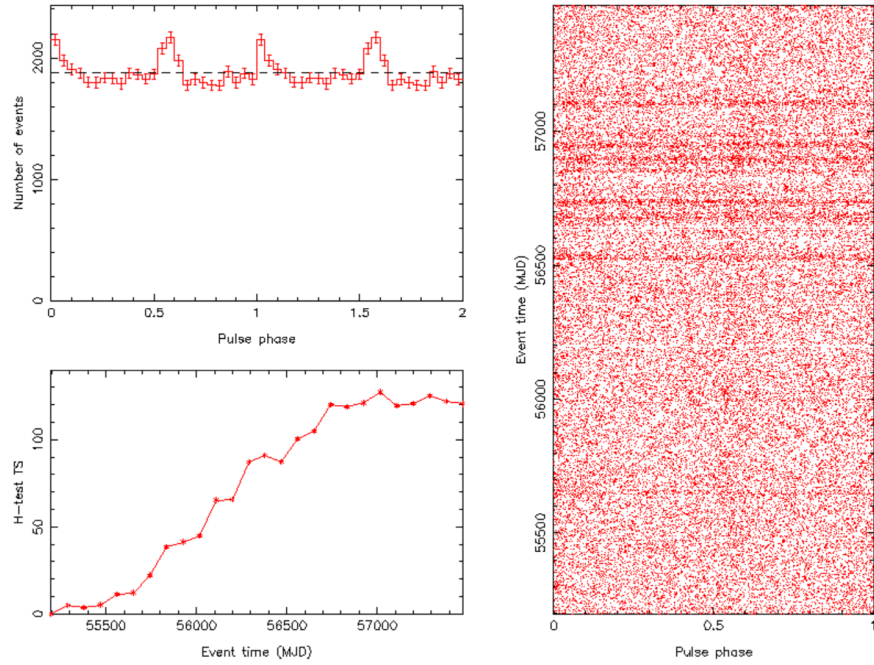


Figure 2.22: Top left panel shows the pulse phase of PSR B1937+21 in gamma-ray band. The figure is produced by tempo2.

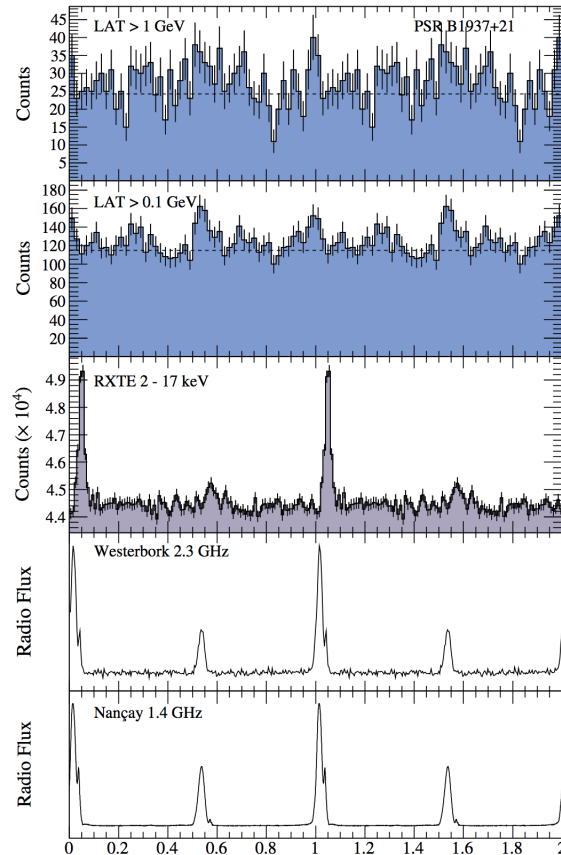


Figure 2.23: Light curves of PSR B1937+21 by different telescopes. The data and figure is from the paper [6]

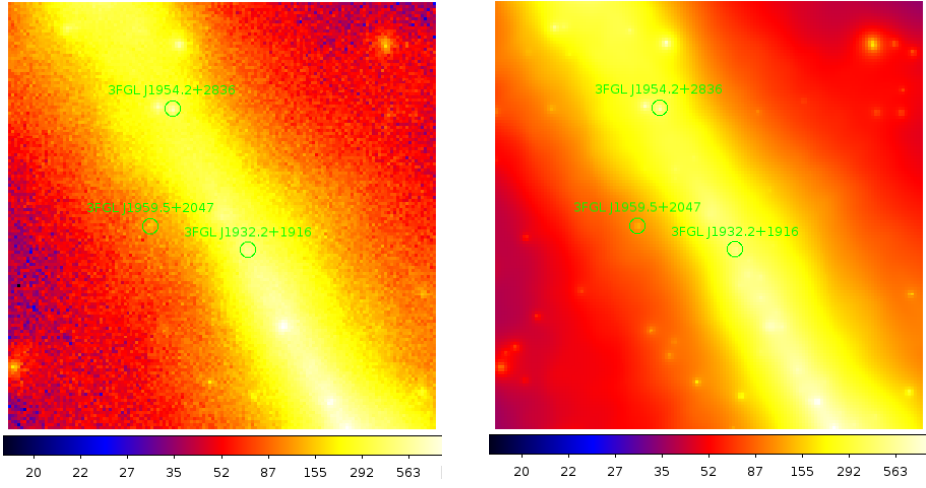


Figure 2.24: The count maps of PSR B1937+21 created from observation data (left) and from the spectral model (right). The dimensions of both figures are  $141\text{pixels} \times 141\text{pixels}$  and each pixel's size is  $0.2^\circ \times 0.2^\circ$ .

### Count Maps and Count Cubes

There are four point sources with free parameters in the model which are represented by the green circles in Figure 2.24 and I add the PLExpCutoff model for PSR B1937+21 manually.

Like the phase-averaged case, the count map is so messy that the source PSR B1937+21 is completely not identifiable in this count map. Figure 2.25 shows count maps in different energy bands. As the figure shows, the lower energy band is very messy while there is no valuable data in the high energy band. Therefore, the data in the middle energy range is more reliable and when fitting the two-layer model, it has higher priority to minimize the differences between the model and observation data in the middle part.

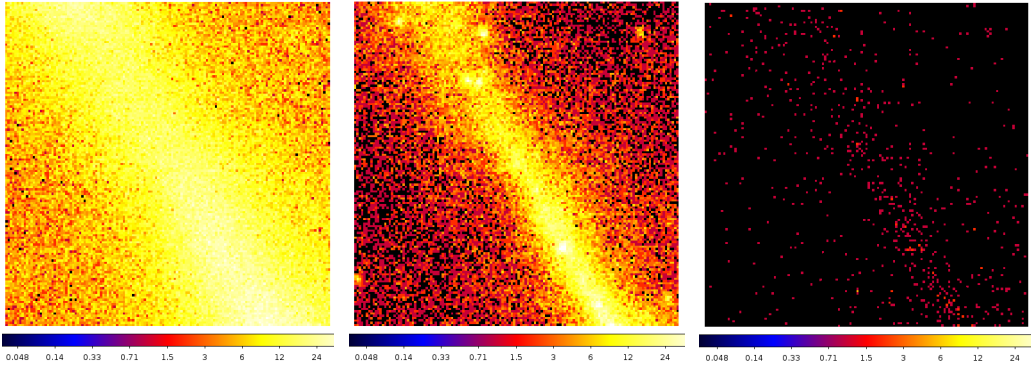


Figure 2.25: Three count maps of PSR B1937+21's count cube. The energy ranges of the figures are from 100 to 126 MeV, from 1.99 to 2.51 GeV, from 50.12 to 63.10 GeV respectively.

### Binned Likelihood Analysis

Figure 2.26 is a combination of the residual map the original count map of PSR B1937+21 in linear scale. The fact that there are many bright dots in the residual map implies that the global fit is not as good as the other two pulsars. Furthermore, the fit is particularly bad in the cyan circle region in the right bottom part Figure 2.26. The total numbers of counts of the cyan region are 18975 and 4212 respectively for the count map and the residual map. The center of the region is  $(290.53^\circ, 14.12^\circ)$  and is about  $8.65^\circ$  away from the source, which means that parameters of the sources in the region are fixed during the fit. This may be the problem of the method of choosing the phase. Firstly I get the pulse phase of PSR B1937+21 and select 40% of the whole rotation period containing the pulse phase. At the same time, I need to change the scales to 40% of their original values for the sources with no free parameters. This is reasonable, however, for some bright sources, a little difference in percent can cause big residuals of photon counts. <question>Not Sure</question>

The Figure 2.27 is the combination of count spectra for all sources within the  $20^\circ$  and the count residual plot. The count residual plot shows that except low gamma-ray energy part (from 100MeV to 200MeV), the total number of

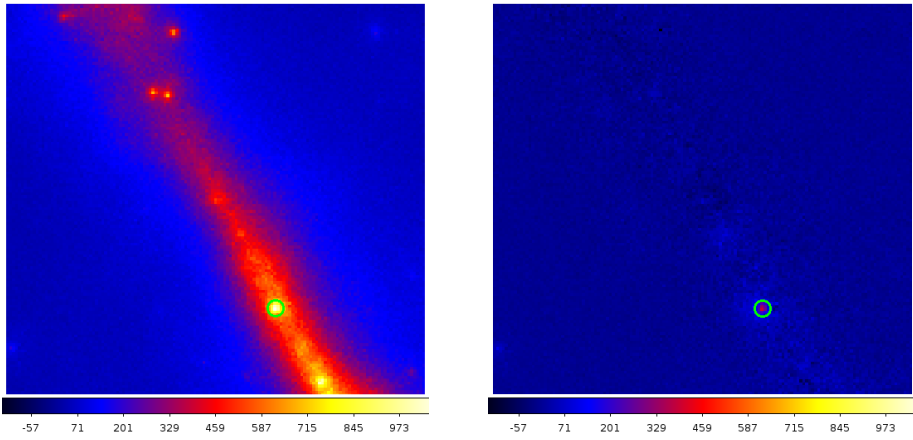


Figure 2.26: The count maps of PSR B1937+21 created from observation data (left) and from the spectral model (right). The dimensions of both figures are  $141\text{pixels} \times 141\text{pixels}$  and each pixel's size is  $0.2^\circ \times 0.2^\circ$ .

photon counts of the model is very close to the observation data. This seems good, but can also imply some problems. As previously discussed, the modeled number of photon counts in the cyan circle is 7924 smaller than the observation data. And the count residual plot shows that the count number of the whole map is nearly the same, which means that in the model there must be some sources forced to be larger than the real value to make up for the deficiency. This implies that the fit results of some sources with free parameters are not as good as the Figure 2.27 shows.

Table 2.8 lists the results of the fit parameters of PSR B1937+21. We see from the table that the new fit results are consistent with the old ones and the precision improves a lot. Figure 2.28 is a plot of the PLExpCutoff model. The global fit is consistent with flux points fitted by each energy bin separately as the flux points and the red line with shade shows. Surprisingly, the power-law model is very close to the phase-resolved PLExpCutoff model. The TS value of our target source is 383, which gives us a significance level  $\sigma \approx \sqrt{TS} = 19.6$ . This implies the presence of the target source. We can also use a TS map to test the presence of the source as Figure 2.29 shows.

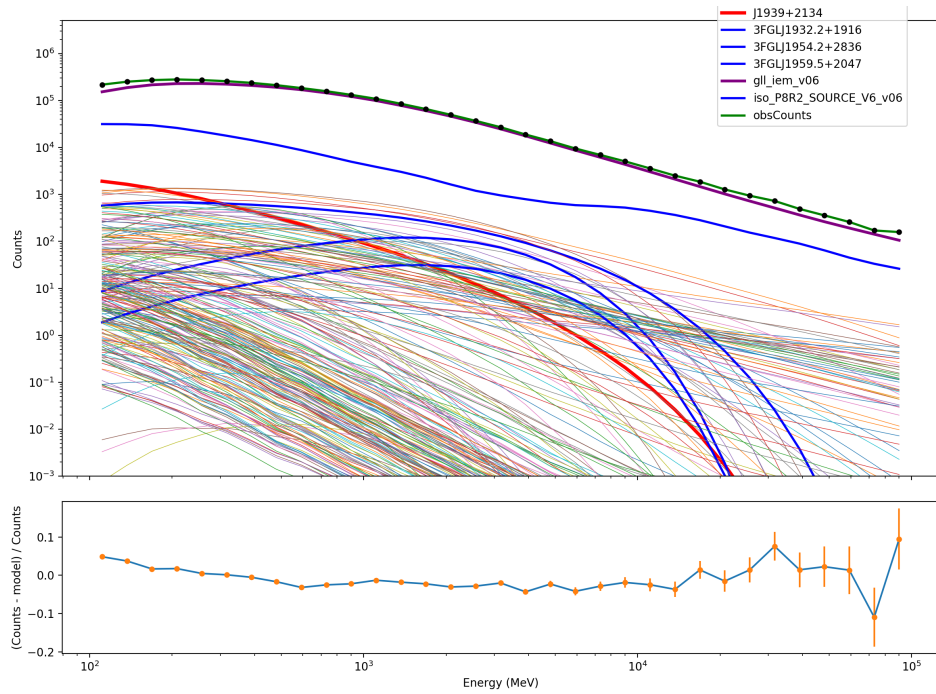


Figure 2.27: The count spectra (top) of all sources including those with only fixed parameters and count residuals (bottom) of the fit for PSR B1937+21.

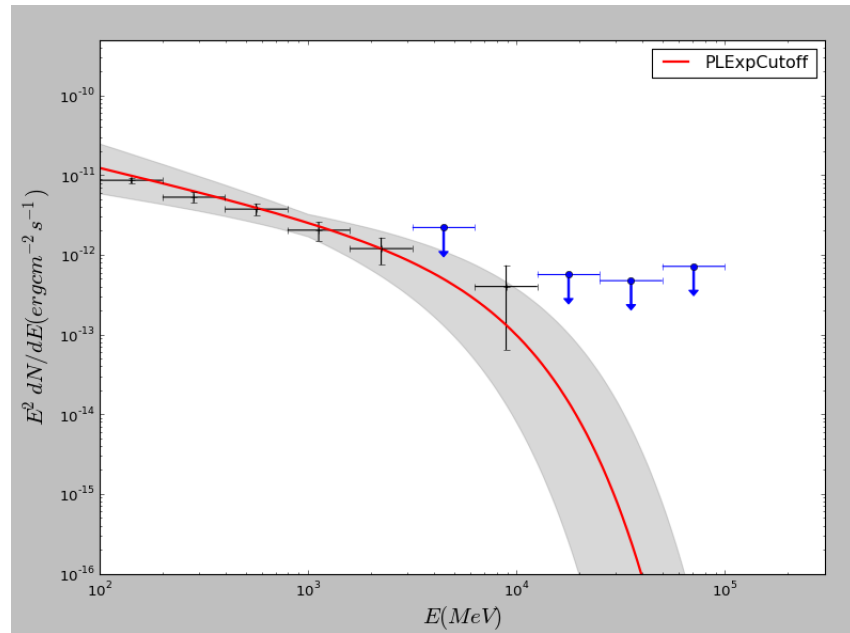


Figure 2.28: PLExpCutoff model spectrum of PSR B1937+21 (phase resolved).

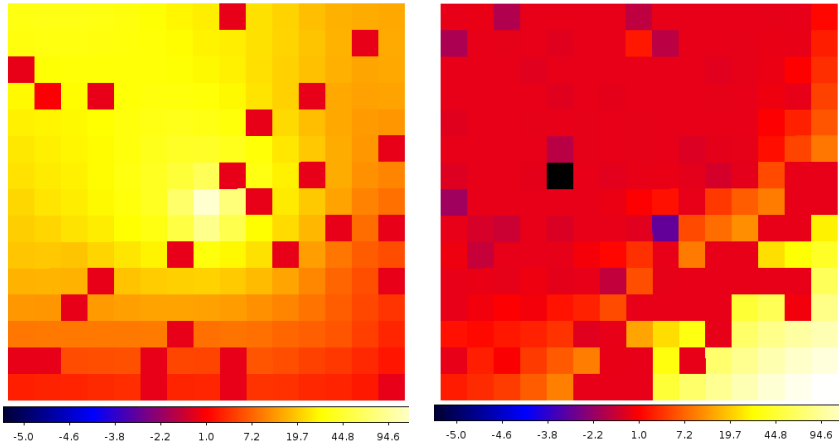


Figure 2.29: TS maps of PSR B1937+21. The dimension is  $3^\circ \times 3^\circ$  (15 pixels  $\times$  15 pixels and each pixel is  $0.2^\circ \times 0.2^\circ$ ). The left panel is generated by the model after removing PSR B1937+21 while the right panel contains the source.

	This Study	Previous Results
Photon Index ( $\Gamma$ )	$2.37 \pm 0.06$	$1.43 \pm 0.87$
Cutoff ( $E_c$ , GeV)	$4.5 \pm 1.2$	$1.15 \pm 0.74$

Table 2.8: Fit parameters of the spectral model of PSR B1937+21 (phase resolved). The previous results are from the paper [11]. Since the studied energy range is different, I do not list the energy flux for comparison.

# Chapter 3

## Theory and Simulation

### 3.1 A Brief Introduction to Outer Gap Model

It is oversimplified to regard a pulsar as a magnetized sphere rotating in vacuum. Actually, there are plenty of charged particles in a pulsar's magneto-sphere which co-rotate with the pulsar. The creation of charged particles can be described following steps [14].

The co-rotating charged primary particles emit gamma-ray by curvature radiation because they are accelerated by environmental magnetic fields. In intense magnetic field, the high energy photons decay into electrons and positrons which are called secondary particles by the process:  $\gamma + (B) \rightarrow e^+ + e^- + (B)$  and these charged particles can emit synchrotron radiations. The secondary particles in charge-deficient regions can also be accelerated to very high speed by strong magnetic field just like primary particles and some of them then emit gamma-rays which can further decay into electrons and positrons. As a result, these charged particles can create more secondary particles. This chain of process is quite efficient to produce charged particles and

make a pulsar's magnetosphere filled with plasma as a consequence. Therefore, a characteristic charge density  $\rho_{GJ} = -\frac{\vec{\Omega} \cdot \vec{B}}{2\pi c}$  called Goldreich-Julian charge density is produced [4]. By the definition of  $\rho_{GJ}$ , there is a surface called null charge surface where  $\rho_{GJ}$  is very close or equal to 0.

Since the charged particles cannot move along the magnetic field lines near the light cylinder, there are closed field lines and open field lines. Charged particles can move out of the magnetosphere along those open field lines. Thus, the charge density in the regions near the light cylinder can be much smaller than Goldreich-Julian charge density and electrons and positrons are accelerated to very high speeds by electric fields parallel to the magnetic field lines ( $E_{||}$ ). These regions are called outer gap which are between the null charge surface and the light cylinder. [3]

Since electrons and positrons are accelerated to opposite directions, there are many charged particles move toward the pulsar's surface. As discussed above, there is no significant electric field to accelerate the incoming particles, they emit softer photons than the photons emitted by the particles move outward. Furthermore, since the softer photons are close the the stellar surface, they can generate electrons and positrons under high magnetic fields. These charged particles maintain the current moving along the open field lines. Meanwhile, the particles moving from null charge surface to the light cylinder are largely accelerated by  $E_{||}$ , and hence emit gamma-rays by curvature radiations. Part of the gamma-rays covert to electron-positron pairs by colliding with soft photons, and the pairs compensate the deficit of charge densities, hence stop the growth of outer gap. This is the very basic introduction of the outer gap model, which is helpful to understand the two-layer model.

## 3.2 Two-layer Model

After we have reviewed gamma-ray emission mechanism, we can proceed to the two-layer model on which this thesis is mainly based [16]. Two-layer model is a variation of outer-gap model since they both claim that the gamma-ray emission zone is close to the light cylinder. However, in the two-layer model, the outer layer consists of two regions — a primary acceleration region and a screening region.

In the primary region, charged particles moved out of pulsars along the open field lines, so the charge density is usually very low. However, by pair-production processes, a lot of  $e^-$  and  $e^+$  are produced. But in the primary region where lots of pairs are created, the charge density doesn't change very much because the pairs have not been separated yet. With the help of strong electric field, the particles of different signs move to opposite directions. As a result, the two-layer model states that above the primary region, a screening region will be created and the charge density is very large because of the accumulation of the charged particles. This is basically the reason why there are two regions in pulsars' outer magnetosphere.

The next issue is that how to describe the distribution of charge density in these two regions. For simplicity, the model just uses a step function to represent the charge density distribution and a step function can clearly shows the gap between the two regions. It uses a magnetic dipole model to approximate the magnetic distribution in the magnetosphere. Since in magnetic dipole model, magnetic fields at one position is only dependent on the position's distance from the source and altitude, the model also ignores the azimuthal distribution of charge density and uses two parameters which are distance  $r$

and altitude  $\theta$  to calculate the magnetic field at a particular position.

The two-layer model uses three parameters to express the structure of a pulsar's outer magnetosphere — charge density of the primary region, the total height of the primary region and the screening region and the last one is the ratio of the thickness of the primary region and the screening region. Figure 3.1 shows the basic structure of two-layer model.

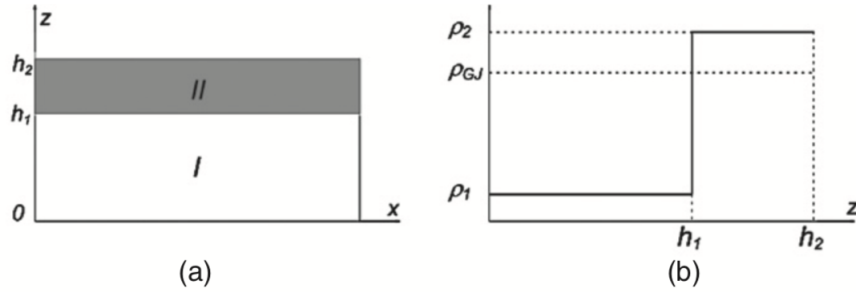


Figure 3.1: (a): Geometry of the two-layer model.  $h_1$  and  $h_2$  is the height of the primary region and the screening region respectively. (b): the charge densities of primary region and screening region. In the primary region, the charge density is much smaller than Goldreich-Julian charge density while is larger in the screening region. The figure is from [16].

As Figure 3.1 shows, let the charge density of the primary region be  $\rho_1 = (1 - g_1)\rho_{GJ}$  and the total gap size be  $h_2$ , where  $\rho_{GJ}$  is the Goldreich-Julian charge density. For convenience, also denote the gap size of the primary region by  $h_1$ .

Denote the electrical potential with  $\phi_0$  which satisfies

$$\nabla^2 \phi_0 = -4\pi\rho_{GJ} \quad (3.1)$$

and the total electrical potential is  $\phi = \phi_0 + \phi'$ , where  $\phi'$  is a representation of the deviation of the co-rotating electrical potential. Let the total charge

density be  $\rho$  and subtract Equation 3.1 we have,

$$\nabla^2 \phi' = -4\pi (\rho - \rho_{GJ}) \quad (3.2)$$

Because the model has ignored the distribution in the azimuthal direction, it uses two parameters  $x, z$  to represent a position, where  $x$  is the direction along the magnetic field line and  $z$  is perpendicular to the magnetic field line. In order to solve Equation 3.2, the model also makes two approximations. The first is that the derivative of electrical potential  $\phi$  is ignored. The second is that the Goldreich-Julian charge density is uniformly distributed along the magnetic line direction ( $x$  direction). These two approximations are based on a reasonable assumption that the change rate for both electrical potential ( $\phi'$ ) and Goldreich-Julian charge density ( $\rho_{GJ}$ ) along the  $x$  direction is much smaller than  $z$  direction. As a result, Equation 3.2 can be written as:

$$\frac{\partial^2}{\partial z^2} \phi' = -4\pi (\rho - \rho_{GJ}) \quad (3.3)$$

In order to solve Equation 3.3, proper boundary conditions are also needed. First of all, we have to decide the boundary positions, which is determined by four parameters and they can be written as  $x_{lo}, x_{hi}, z_{lo}, z_{hi}$ . It is reasonable to set  $x_{lo}$  and  $x_{hi}$  be the pulsar's surface and the light cylinder respectively and  $z_{lo}$  (lower boundary) be the last open field line. And let the electrical potential be 0 along the last open field line (this is because the variation of electric field in  $x$  direction is ignored).

$$\phi(x, z_{lo}) = 0 \quad (3.4)$$

To know the position of  $z_{hi}$  is a little bit tricky. In order to make the electrical

potential be continuous at  $z = z_{hi} = h_2$ , the model sets the  $\phi'(z = h_2) = 0$  since the non-co-rotating electrical potential outside the upper bound is 0 and the co-rotating potential is continuous near the boundary. Additionally, because  $\phi'(z = h_2-) = 0$  and  $\phi'(z = h_2+) = 0$ , it is known that the first derivative  $\partial\phi'/\partial z|_{z=h_2}$  is 0, which means  $E_\perp|_{z=h_2} = 0$ . In order to solve Equation 3.3, denote charge densities of the two regions for convenience as the function 3.5 shows.

$$\rho(z) = \begin{cases} \rho_1, & \text{if } (0 \leq z < h_1) \\ \rho_2, & \text{if } (h_1 \leq z \leq h_2) \end{cases} \quad (3.5)$$

With definition in Equation 3.5 and the three boundary conditions, the solution of Equation 3.3 is,

$$\phi'(z, x) = -2\pi \begin{cases} (\rho_1 - \rho_{GJ}(x)) z^2 + C_1 z, & (0 \leq z < h_1) \\ (\rho_2 - \rho_{GJ}(x)) (z^2 - h_2^2) + D_1 (z - h_2), & (h_1 \leq z \leq h_2) \end{cases} \quad (3.6)$$

where

$$C_1 = \frac{(\rho_1 - \rho_{GJ}(x)) h_1 (h_1 - 2h_2) - (\rho_2 - \rho_{GJ}(x)) (h_1 - h_2)^2}{h_2}$$

and

$$D_2 = \frac{(\rho_1 - \rho_2) h_1^2 - [\rho_2 - \rho_{GJ}(x)] h_2^2}{h_2}$$

From Equation 3.6 and apply  $\rho_{GJ}(x) = -(\Omega B x) / (2\pi c s)$  we can directly derive the electrical field parallel to magnetic field lines as a function of  $z$  as Equation 3.7 shows.

$$E'_\parallel(z) = \frac{\Omega B}{c s} \begin{cases} -g_1 z^2 + C'_1 z, & (0 \leq z < h_1) \\ g_2 (z^2 - h_2^2) + D'_1 (z - h_2) & (h_1 \leq z \leq h_2) \end{cases} \quad (3.7)$$

where

$$C'_1 = \frac{g_1 h_1 (h_1 - 2h_2) + g_2 (h_1 - h_2)^2}{h_2}$$

and

$$D'_2 = -\frac{(g_1 + g_2) h_2^2 + g_2 h_2^2}{h_2}$$

Since charged particles are accelerated in the primary region to relativistic speeds and then emit energy by curvature radiation, we have,

$$eE'_{\parallel}c = l_{cur} \quad (3.8)$$

where  $E'_{\parallel}$  is the electric field strength along the magnetic field line described in Equation 3.7. Lorentz factors of the charged particles is estimated according to Equation 3.9.

$$l_{cur} = \frac{2e^2 c \gamma_e^4}{3s^2} \quad (3.9)$$

where  $s$  is the radius of curvature. Combining Equation 3.8 and Equation 3.9 we get expression for Lorentz factor:

$$\gamma_e = \left( \frac{3s^2}{2e} E'_{\parallel} \right)^{1/4} \quad (3.10)$$

With Lorentz factor of charged particles known, we can derive curvature radiation spectrum for single charged particle and then can get the total spectrum by integrating over all charged particles. This is the simplified idea of the Two-layer model.

### 3.3 Numerical Calculation of Spectra Based on Two-layer Model

After we have understood the theory part of the two-layer model, we can then do numerical calculations of the spectra based on the theory. Since the theory is the same for all the three MSPs, the calculation algorithms are the same.

There are three independent parameters to fit altogether in the calculation. The first parameter is fractional gap size  $f = h_2/R_{lc}$ , where  $h_2$  is the total gap size including both the primary acceleration region and the screening region and  $R_{lc}$  is the length of light cylinder. The second parameter is  $g_1$  so that the charge density in the primary accelerating region is  $(1 - g_1) \rho_{GJ}$ , where  $\rho_{GJ}$  is the Goldreich-Julian charge density. The third parameter is the ratio between the sizes of the two gaps ( $h_1/h_2$ ). Note that we only set the charge density in the primary acceleration region as an independent parameter, since the charge density in the two gaps are related to each other. Figure 3.2 is the spectra of the three MSPs generated from the two-layer model and the result of the fitting parameters are listed in Table 3.1. Other than the low energy and high energy gamma-ray bands, the model is consistent with the observation data in terms of gamma-ray part.

Generally speaking, the modeled spectra for the three MSPs are acceptable. Just as we have discussed in the data analysis part that global fits are not very consistent with separate fits in low energy gamma-ray band (about 100MeV – 1000MeV) and high energy band (above 10GeV), the modeled spectra also have the same problem. This can have two explanations. Firstly, the Fermi telescope is not sensitive below about 100MeV. As a result, the observation data may not be very reliable at this energy band. Secondly, the real emission

mechanism in the energy band is different from the model predicts. Thus, we can observe inconsistency between the calculations and observations.

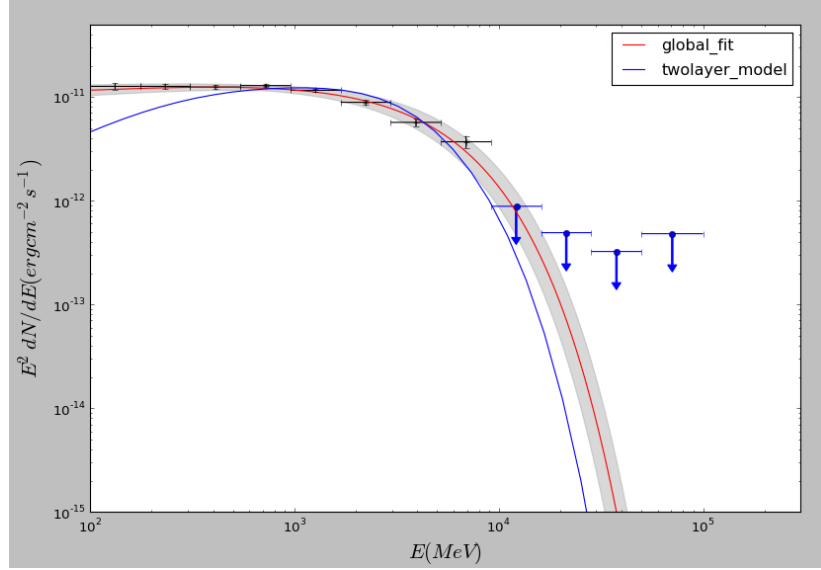


Figure 3.2: The modeled spectrum of PSR J0218+4232.

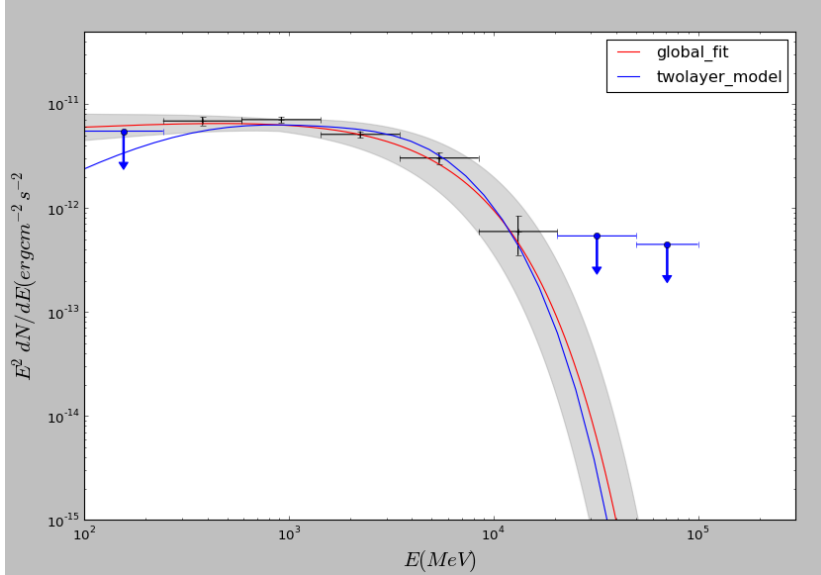


Figure 3.3: The modeled spectrum of PSR B1821-24.

After obtaining the spectra fit results in gamma-ray band, we can generate broad band spectra as Figure 3.5 shows. The hard X-ray data are from the paper [5]. By tweaking the independent parameters of the two-layer model, we can make the modeled spectra very close to the observation data in hard X-ray

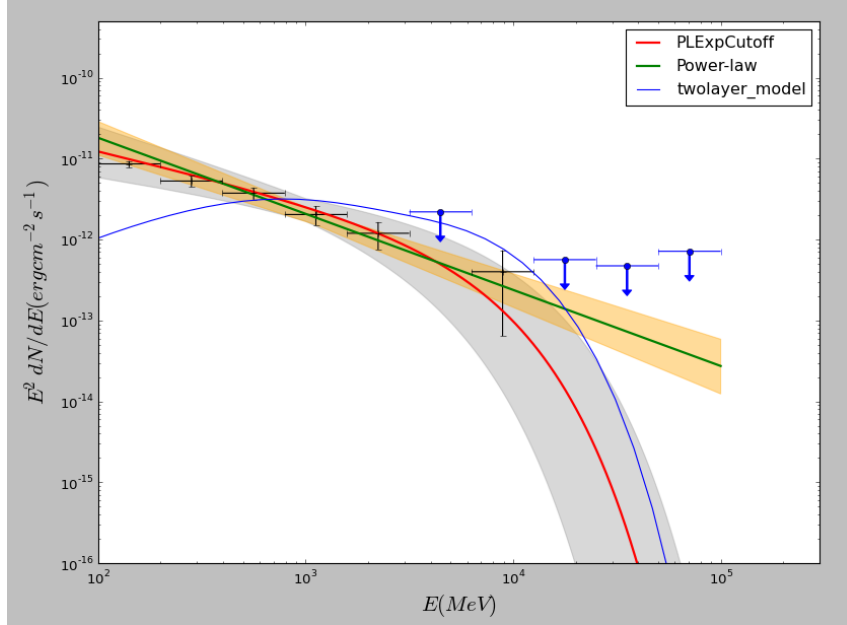


Figure 3.4: The modeled spectrum of PSR B1937+21.

	f	g	$h_1/h_2$
PSR J0218+4232	0.330	0.92	0.915
PSR B1821-24	0.247	0.955	0.920
PSR B1937+21	0.320	0.975	0.925

Table 3.1: The results of fitting parameters for the three MSPs. The physical meaning of each parameter is consistent with the two-layer model described above.

band. Since we lack observation data in the energy band from about 100keV to 100MeV, we cannot tell if the two-layer model describes the right physical scenario in this energy range. However, the prediction made by the simplified two-layer model is relatively precise. In addition, the model is very intuitive, which is also a very important consideration for building a model. Just as the famous words "With four parameters I can fit an elephant, and with five I can make him wiggle his trunk" said by John von Neumann, in principle, we can fit any data by adding independent parameters. Therefore, in order to test if a theory model is good or not, not only we need to consider how precisely the model can predict, but also the physical meaning behind the model. In this

sense, the two-layer model is a good start of explaining emission mechanism of pulsars.

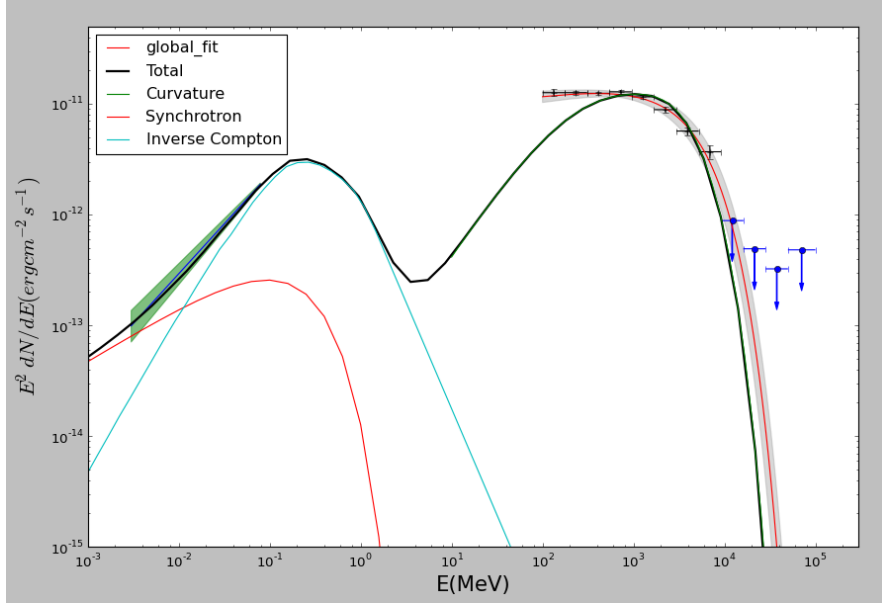


Figure 3.5: The broad band and modeled spectrum of PSR J0218+4232. The grey shade is the error of the global fit. And the green shade in the left panel of the figure represents the error of hard X-ray. The 'Total' legend represents the total flux combining the Synchrotron radiation, inverse Compton radiation and curvature radiation altogether.

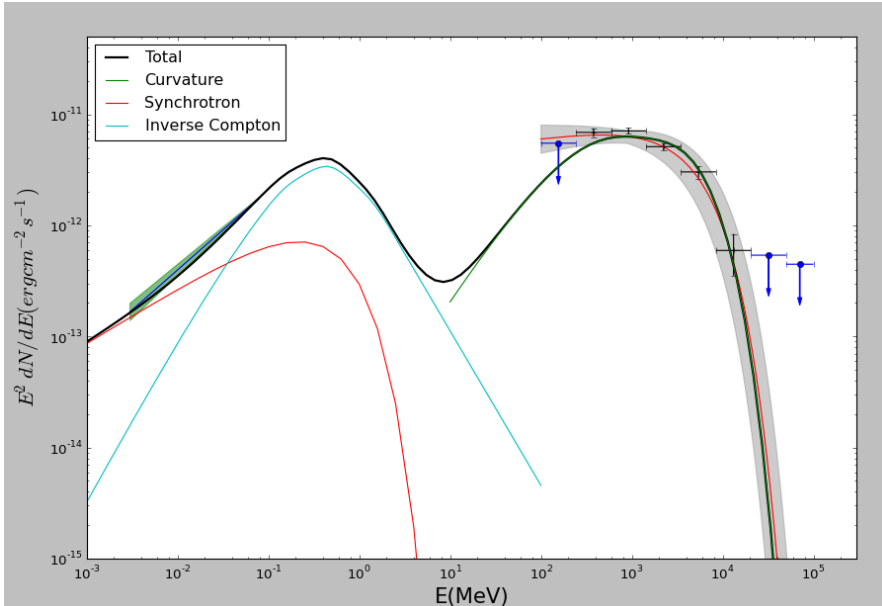


Figure 3.6: The broad band and modeled spectrum of PSR B1821-24. The meaning of grey shade and the green shade are the same as Figure 3.5

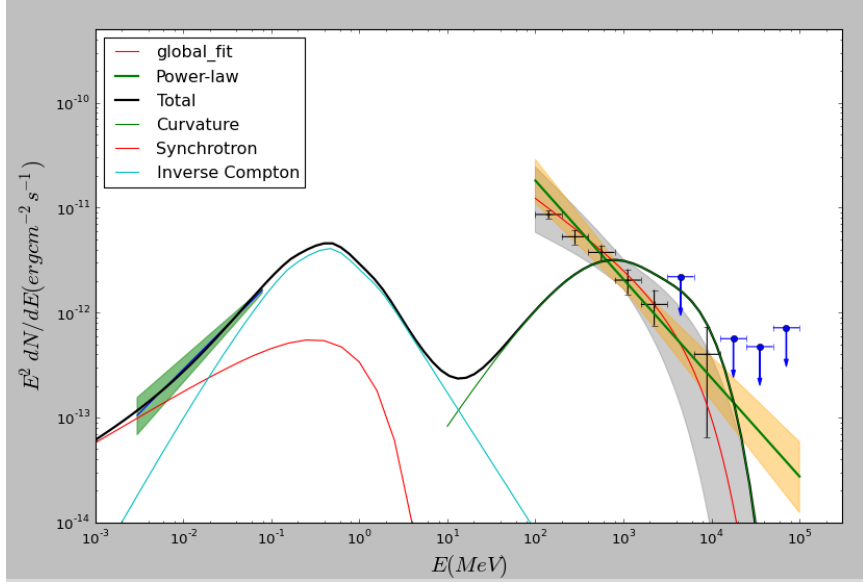


Figure 3.7: The broad band and modeled spectrum of PSR B1937+21. The meaning of grey shade and the green shade are the same as Figure 3.5

## 3.4 Pitfalls and Considerations of Doing Numerical Calculation

### 3.4.1 Correctness of Computation

To make sure the numerical computation be right is the most important. The first consideration is underflow and overflow of floating digits. One possible condition is calculating speed of relativistic charged particles with Lorentz factor  $\gamma$ . By doing some simple test, we find that for  $\gamma < 1.5 \times 10^7$ , the results are precise enough. However, there is significant rounding error when  $\gamma > 5 \times 10^7$ , which means that our results will be wrong for highly energetic particles if we directly use the formula  $\beta = \sqrt{1 - 1/\gamma^2}$ . Likely, in the two-layer model, nearly all particles have  $\gamma < 1 \times 10^7$ . Furthermore, there are nearly no situations where double precision floating digits cannot handle calculation results of the two-layer model. Thus, as long as we use 64-bit floating digits

instead of 32-bit floating digits, we are free from overflowing and underflow troubles.

There are some cases when a whole function can be calculated while some parts of them are not. Take Function  $f(x) = x \times 1/x$  for example. When  $x$  is too large, it can not be expressed by a computer and multiplication is not associative when doing floating point operation. We encounter some situations like this. The formula of curvature radiation spectrum contains modified Bessel function of order 5/3. In order to speed up the program, we use a polynomial to express the Bessel function, as Equation 3.11 shows.

$$K_{5/3}(x) \simeq a \left( \frac{1}{x} + b \right)^{-cx-1/3} \sqrt{\frac{\pi}{2}} e^{-x-d} \sqrt{x+d} \left[ 1 + \frac{55}{72(x+d)} - \frac{10151}{10368} (x+d)^2 \right] \quad (3.11)$$

where  $a, b, c, d$  are just positive constants and  $c = 0.96 < 1$ . As a result, the part  $(1/x + b)^{-cx-1/3}$  in Function 3.11 is infinity when  $x$  is large though the total function is approximated to 0. Thus, we have to explicitly assign the result to be 0 instead of calculating it. Actually, this error is not easy to find since in most cases the result is not infinity.

### 3.4.2 Speed of Computation

We actually have not done any accurate benchmarks for the following discussions and they are dependent of the average time of running the simulation. The most obvious solution of to use multicores to do computation. However, most library functions do not support run concurrently and only run on a single core. For example, we need to do many integrations and the speed of integration is critical. We write some simple functions to utilize four CPU cores at the same time when doing integration. This gives us a huge performance improvement.

Furthermore, There are some facts about the basic operations. For instance, add is faster than multiplication which is faster than devision. Multiplications and devisions are not associative between floating points. Though the performance differences between different operations for integers can usually be optimized away by modern compilers, the compilers can do nothing for floating points. Thus, we have to do it by ourselves. For example, we have  $z^2 - h_2(x)^2$  in function 3.7. In this formula, we have two multiplications and one subtraction. After we re-write it to  $(z - h_2)(z + h_2)$ , we have one addition, one subtraction and one multiplication. Since addition and subtraction is not slower than multiplication, it has no performance harm for the rewriting. What we need to notice is that the multiplication may not be slower than addition and it is dependent on machines. However, division is definitely slower than the other three operations. Therefore, in our program, expressions like  $1/3$  are rewritten to  $1 * 0.3333$  and so on.

# Chapter 4

## Conclusion

The spectra of PSRs J0218+4232, B1937+21 and B1821-24 are studied using more observation data and newly published *Pass 8* dataset. The new results of the thesis are generally consistent with the old results as the Table 4.1 shows. For PSR B1937+21, I also list the results of power-law model as Table 4.2 shows.

	J0218+2134		B937+21		B1821-24	
	New	Previous	New	Previous	New	Previous
Photon Index $\Gamma$	$1.89 \pm 0.04$	$2.0 \pm 0.1$	2.61	$1.43 \pm 0.87$	$1.91 \pm 0.07$	$1.6 \pm 0.3$
Cutoff Energy (GeV)	$3.77 \pm 0.40$	$4.6 \pm 1.2$	$4.90 \pm 0.30$	$1.15 \pm 0.74$	$4.50 \pm 0.71$	$3.3 \pm 1.5$
Photon Flux ( $10^{-8} \text{ cm}^{-2}\text{s}^{-1}$ )	$7.29 \pm 0.28$	$7.7 \pm 0.7$	$3.76 \pm 0.35$		$3.85 \pm 0.31$	$1.5 \pm 0.6$
Energy Flux ( $10^{-11} \text{ erg cm}^{-2}\text{s}^{-1}$ )	$4.45 \pm 0.16$	$4.56 \pm 0.24$	$1.58 \pm 0.15$		$2.44 \pm 0.14$	$1.3 \pm 0.2$

Table 4.1: Fit parameters of the spectral model of PSR J0218+4232. The names of parameters are consistent with Equation 2.4. The previous results are from the paper [2].

With *Pass 8* data and more observation data, the new results have smaller error bars in terms of photon index and energy flux. Further more, we have much larger TS values for PSRs J0218+4232 and PSRs B1821-24 as the Table

	New Results	Previous Results
Photon Index ( $\Gamma$ )	$2.94 \pm 0.13$	$2.38 \pm 0.07$
Photon Flux ( $10^{-8} \text{ cm}^{-2}\text{s}^{-1}$ )	$5.89 \pm 0.68$	2.93
Energy Flux ( $10^{-11}\text{erg cm}^{-2}\text{s}^{-1}$ )	$1.92 \pm 0.18$	$1.6 \pm 0.2$
TS value	147	112

Table 4.2: Fit results of power-law model for PSR B1937+21. Since the previous paper does not show the photon flux, I cannot calculate the error bars of photon flux for the previous value.

4.3 shows. For PSR B1937+21, a power-law model should be preferred because of the following reasons. The  $-\log(\text{likelihood})$  of PLExpCutoff model and power-law model are  $-4410944$  and  $-18409504$  respectively, the  $TS_{cut} = 2\Delta\log(\text{likelihood}) = -2.86 < 9$ , thus I follow the convention of the paper [1].

	J0218+4232	B1821-24	B1937+21
Previous	1313	76	112
New Results	6809	941	147

Table 4.3: TS values comparison between the new results and the previous results for the three MSPs.

Although the two-layer model introduced in the thesis is simplified very much, its prediction of broad-band spectra (including hard X-ray and gamma-ray) for the three energetic MSPs are generally acceptable, except that for the energy of a few hundred MeV.

# Chapter 5

## Discussion and Future Work

### 5.1 Constraints of The Two-layer Model Used In The Thesis

The simplified two-layer model is consistent with observation data to some extent. (The relevant data can be found in the paper [16]) The model uses four parameters to get a fairly good prediction of the gamma-ray spectra of many pulsars. And all these four parameters have very obvious physical meanings. However, the problems of the model is clear — it is somewhat oversimplified. Although there are other more sophisticated versions of the two-layer model such as three-dimensional two-layer model [17] and I used the simpler one, which may cause some inconsistencies between the simulations and observations.

Therefore, we can briefly analyze which part is oversimplified and can be improved. First of all, we directly use a step function to describe the charged particle distribution. Though the charge density of the screening region is

much larger than the primary region, using a step function is not very physical and may exaggerate the change rate of charge density. At the same time, the dramatic change of charge density also brings some numerical instabilities.

Secondly, the model sets the total of screening region and primary region to be rectangular shape. Though the actual shape is not clear, it should not be a rectangle in theory and may be very different. In numerical simulation, changes in shape of the regions will directly lead to a different integration region, which may change the simulated spectra.

Thirdly, there are some inconsistencies in the model itself according to its assumptions. According to Equation 3.9 and Equation 3.10, since  $E'_{\parallel}$  can be 0, we know that  $\gamma_e$  can also be 0, which is absolutely non-physical. Although this may not have large influences on the spectra, it is the problem that should be avoided.

All in all, the model is simple and the gamma-ray spectra computed based on the model is consistent with observation data. There are many much more sophisticated two-layer model which are generalizations of model used in the thesis. Those models may have addressed the problems described above, but the model used in the thesis do have some defects.

## 5.2 Inconsistency Between the Two-layer Model and Fit Results

As Figures 3.5, 3.7 and 3.6 show, the two-layer model and the global fit for all the three MSPs are not consistent with each other in lower gamma-ray bands (about 100 MeV). I have tried different reasonable parameter combinations to

fix the problem, but it is not solved. I think there could be some reasonable explanations. First of all, the energy resolution of *Fermi Lat* in a few hundred MeV is not as good as in other gamma-ray bands. Secondly, energy band of several hundred MeV, the signal-to-noise is low compared with high energy part. By directly analyzing the events files, we find that about 90% of photons are in 100MeV to 1000MeV and the background is too bright compared with the target sources. Finally, the two-layer model used in the thesis are oversimplified. In most cases, the spectrum produced by the theory model is not monotone and curved very much. However, the global fits of the PLExp-Cutoff model are usually very flat from 100MeV to 500MeV. This means that even though regardless of physical meanings, no matter what parameter combinations I choose, I can hardly get the similar shape in this energy range. Therefore, I think the simplified version of two-layer model used in the thesis (there are other more sophisticated two-layer models) cannot do a precise prediction in this energy range.

### 5.3 Analysis With *LAT 8-year Point Source List*

The latest preliminary *LAT 8-year Point Source List (FL8Y)* is released on 03 May 2018. Since the release date is a little bit late and the point source list is a preliminary version, I have not finished the spectra analysis with the data. However, it is reasonable to show some results I have done with the new source list and my further plan.

Some spectra models are changed, for instance, *PLSuperExpCutoff* model is removed and *PLSuperExpCutoff2* is added. The

equation of `textit{PLSuperExpCutoff2}` [9] is,

$$\frac{dN}{dE} = K \left( \frac{E}{E_0} \right)^{\Gamma} \exp(a(E_0^b - E^b)) \quad (5.1)$$

In principal, there is no difference between the Equations 2.4 and 5.1, the parameters needed to be fitted is different. In fact, the *Cutoff* in *PLSuperExpCutoff* is changed to *Expfactor* in *PLSuperExpCutoff2*.

<**add**>continue from here</**add**>

# Bibliography

- [1] A. A. Abdo, M. Ajello, and A. Allafort. The second fermi large area telescope catalog of gamma-ray pulsars. 208:17, Oct 2013.
- [2] A. A. Abdo, M. Ajello, A. Allafort, L. Baldini, J. Ballet, G. Barbiellini, M. G. Baring, D. Bastieri, A. Belfiore, R. Bellazzini, B. Bhattacharyya, E. Bissaldi, E. D. Bloom, E. Bonamente, E. Bottacini, T. J. Brandt, J. Bregeon, M. Brigida, P. Bruel, R. Buehler, M. Burgay, T. H. Burnett, G. Busetto, S. Buson, G. A. Calandro, R. A. Cameron, F. Camilo, P. A. Caraveo, J. M. Casandjian, C. Cecchi, Ö. Çelik, E. Charles, S. Chaty, R. C. G. Chaves, A. Chekhtman, A. W. Chen, J. Chiang, G. Chiaro, S. Ciprini, R. Claus, I. Cognard, J. Cohen-Tanugi, L. R. Cominsky, J. Conrad, S. Cutini, F. D’Ammando, A. de Angelis, M. E. DeCesar, A. De Luca, P. R. den Hartog, F. de Palma, C. D. Dermer, G. Desvignes, S. W. Digel, L. Di Venere, P. S. Drell, A. Drlica-Wagner, R. Dubois, D. Dumora, C. M. Espinoza, L. Falletti, C. Favuzzi, E. C. Ferrara, W. B. Focke, A. Franckowiak, P. C. C. Freire, S. Funk, P. Fusco, F. Gargano, D. Gas-parrini, S. Germani, N. Giglietto, P. Giommi, F. Giordano, M. Giroletti, T. Glanzman, G. Godfrey, E. V. Gotthelf, I. A. Grenier, M.-H. Grondin, J. E. Grove, L. Guillemot, S. Guiriec, D. Hadash, Y. Hanabata, A. K. Harding, M. Hayashida, E. Hays, J. Hessels, J. Hewitt, A. B. Hill, D. Horan, X. Hou, R. E. Hughes, M. S. Jackson, G. H. Janssen,

- T. Jogler, G. Jóhannesson, R. P. Johnson, A. S. Johnson, T. J. Johnson, W. N. Johnson, S. Johnston, T. Kamae, J. Kataoka, M. Keith, M. Kerr, J. Knödlseder, M. Kramer, M. Kuss, J. Lande, S. Larsson, L. Latronico, M. Lemoine-Goumard, F. Longo, F. Loparco, M. N. Lovellette, P. Lubrano, A. G. Lyne, R. N. Manchester, M. Marelli, F. Massaro, M. Mayer, M. N. Mazziotta, J. E. McEnery, M. A. McLaughlin, J. Mehault, P. F. Michelson, R. P. Mignani, W. Mitthumsiri, T. Mizuno, A. A. Moiseev, M. E. Monzani, A. Morselli, I. V. Moskalenko, S. Murgia, T. Nakamori, R. Nemmen, E. Nuss, M. Ohno, T. Ohsugi, M. Orienti, E. Orlando, J. F. Ormes, D. Paneque, J. H. Panetta, D. Parent, J. S. Perkins, M. Pesce-Rollins, M. Pierbattista, F. Piron, G. Pivato, H. J. Pletsch, T. A. Porter, A. Possenti, S. Rainò, R. Rando, S. M. Ransom, P. S. Ray, M. Razzano, N. Rea, A. Reimer, O. Reimer, N. Renault, T. Reposeur, S. Ritz, R. W. Romani, M. Roth, R. Rousseau, J. Roy, J. Ruan, A. Sartori, P. M. Saz Parkinson, J. D. Scargle, A. Schulz, C. Sgrò, R. Shannon, E. J. Siskind, D. A. Smith, G. Spandre, P. Spinelli, B. W. Stappers, A. W. Strong, D. J. Suson, H. Takahashi, J. G. Thayer, J. B. Thayer, G. Theureau, D. J. Thompson, S. E. Thorsett, L. Tibaldo, O. Tibolla, M. Tinivella, D. F. Torres, G. Tosti, E. Troja, Y. Uchiyama, T. L. Usher, J. Vandebroucke, V. Vasileiou, C. Venter, G. Vianello, V. Vitale, N. Wang, P. Weltvrede, B. L. Winer, M. T. Wolff, D. L. Wood, K. S. Wood, M. Wood, and Z. Yang. The second fermi large area telescope catalog of gamma-ray pulsars. *The Astrophysical Journal Supplement Series*, 208(2):17, 2013.
- [3] K.S. Cheng, C. Ho, and M. Ruderman. Energetic radiation from rapidly spinning pulsars. i - outer magnetosphere gaps. ii - vela and crab. *The Astrophysical Journal*, 300:500–539, Jan 1986.
- [4] P. Goldreich and W. H. Julian. Pulsar electrodynamics. *The Astrophysical*

*Journal*, 157:869, aug 1969.

- [5] E. V. Gotthelf and S. Bogdanov. Nustar hard x-ray observations of the energetic millisecond pulsars psr b1821-24, psr b1937+21, and psr j0218+4232. *The Astrophysical Journal*, 845(2):159, 2017.
- [6] L. Guillemot, T. J Johnson, and et al. Pulsed gamma rays from the original millisecond and black widow pulsars: A case for caustic radio emission?
- [7] L. Guillemot, T. J. Johnson, C. Venter, M. Kerr, B. Pancrazi, M. Livingstone, G. H. Janssen, P. Jaroenjittichai, M. Kramer, I. Cognard, B. W. Stappers, A. K. Harding, F. Camilo, C. M. Espinoza, P. C. C. Freire, F. Gargano, J. E. Grove, S. Johnston, P. F. Michelson, A. Noutsos, D. Parent, S. M. Ransom, P. S. Ray, R. Shannon, D. A. Smith, G. Theureau, S. E. Thorsett, and N. Webb. Pulsed gamma rays from the original millisecond and black widow pulsars: A case for caustic radio emission? *The Astrophysical Journal*, 744(1):33, 2012.
- [8] O. Hamil, J. R. Stone, M. Urbanec, and G. Urbancová. Braking index of isolated pulsars. *Phys. Rev. D*, 91:063007, Mar 2015.
- [9] B. Lott J. Ballet, T. H. Burnett and the Fermi-LAT collaboration. Fermi-lat 8-year source list.
- [10] T. J. Johnson, L. Guillemot, M. Kerr, I. Cognard, P. S. Ray, M. T. Wolff, G. H. Janssen, R. W. Romani, C. Venter, J. E. Grove, P. C. C. Freire, M. Wood, C. C. Cheung, J. M. Casandjian, I. H. Stairs, F. Camilo, C. M. Espinoza, E. C. Ferrara, A. K. Harding, S. Johnston, M. Kramer, A. G. Lyne, P. F. Michelson, S. M. Ransom, R. Shannon, D. A. Smith, B. W. Stappers, G. Theureau, and S. E. Thorsett. Broadband pulsations from

- psr b1821-24: Implications for emission models and the pulsar population of m28. *The Astrophysics Journal*, 778:106, Dec 2013.
- [11] C.-Y. Ng, J. Takata, G. C. K. Leung, K. S. Cheng, and P. Philippopoulos. High-energy emission of the first millisecond pulsar. *The Astrophysical Journal*, 787(2):167, 2014.
- [12] A. Teoh R. N. Manchester, G. B. Hobbs and Astronomical Journal M. Hobbs. The atnf pulsar catalogue.
- [13] Zakir F. Seidov. The roche problem: Some analytics. *The Astrophysical Journal*, 603(1):283, 2004.
- [14] P. A. Sturrock. A model of pulsars. *Astrophys. J.*, 164:529, 1971.
- [15] Hao Tong. Pulsar braking: magnetodipole vs. wind. *Science China Physics, Mechanics Astronomy*, 59(1):619501.
- [16] Y. Wang, J. Takata, and K. S. Cheng. Gamma-ray spectral properties of mature pulsars: A two-layer model. *The Astrophysical Journal*, 720(1):178, 2010.
- [17] Y. Wang, J. Takata, and K. S. Cheng. Three-dimensional two-layer outer gap model: Fermi energy-dependent light curves of the vela pulsar. *Monthly Notices of the Royal Astronomical Society*, 414(3):2664–2673, 2011.